Prion Propagation and Loss in Single Bacterial Cells

Krista Jager

A thesis
in
The Department
of
Biology

Presented in Partial Fulfillment of the Requirements
For the Degree of Master of Science (Biology)
at Concordia University
Montréal, Québec, Canada

January 2022

Concordia University
School of Graduate Studies

This is to certify that the thesis prepared

By: **Krista Jager**
Entitled: **Prion Propagation and Loss in Single Bacterial Cells**

and submitted in partial fulfillment of the requirements for the degree of

Master of Science (Biology)

complies with the regulations of this University and meets the accepted standards with respect to originality and quality.

Signed by the final examining commitee:

_____ Chair
Dr.

_____ Examiner
Dr. Steve Shih

_____ Examiner
Dr. Michael Hallett

_____ Examiner
Dr. William Zerges

_____ Supervisor
Dr. Laurent Potvin-Trottier

Approved by _____
Dr. Robert Weladji, Graduate Program Director

Date _____ _____
Dr. Pascale Sicotte, Dean of Arts and Science

Abstract

Prion Propagation and Loss in Single Bacterial Cells

Krista Jager

Originally discovered in the context of fatal neurodegenerative diseases, prions are proteins that can exist in two conformations: a normal one and a self-propagating form that can convert native proteins to the prion form. Surprisingly, prion proteins can also act as a stable, non-pathogenic epigenetic switch. The propagation of prion aggregates appears to be conserved across all domains of life, with extremely rare spontaneous transitions between the two conformations. The long timescales involved in prion conversion and loss have limited previous studies, leaving the underlying molecular mechanisms of these transitions still poorly understood. We set up a microfluidic platform that enabled tracking thousands of individual cells using quantitative time lapse fluorescence microscopy as they propagated and lost the prion state in *Escherichia coli* over hundreds of cell divisions. We focused on the recently discovered prion-forming domain in the single-stranded DNA binding protein (SSB) of the bacteria *Campylobacter hominis*, and observed two modes of prion propagation: small aggregates and an ultra-stable large aggregate located at the old pole of the cell. While cells harbouring the large aggregates maintained the prion state, the small aggregate sub-population lost the prion state following exponential decay. We further showed that, in this system, partitioning errors are the main cause of prion loss, and subsequently corroborated these results using orthologous prion domains. As many prion proteins have unknown function, we investigated the general physiological impact of the presence of prions in bacteria. We found that the prions imposed a small cost to the growth rate; however, our preliminary results suggest that they could also provide increased resistance to proteotoxic stresses. Our results emphasize the strengths of using a bacterial model system and our microfluidic setup to study the molecular mechanisms of prion propagation.

Acknowledgments

I would first like to thank my wonderful supervisor, Dr. Laurent Potvin-Trottier, for his continuous support and patience. Thank you for always providing encouragement and dedicated involvement in every step throughout this process. I am honoured to be your first graduating student. A great deal of thanks goes to the GE 3rd floor community and my labmates for creating a fun, positive, and safe environment to learn in. I would like to thank my fabulous officemates Saba, Tina and Paige for always letting me distract them, and for providing emotional support after failed experiments. Thank you Ellie for being my first friend in Montreal, helping me with everything from bench work to coding, and most importantly for making pancakes every Saturday morning when we lived together.

I am extremely grateful for the love and support from my friends outside the lab. Thank you Liz, for always being available for a call or virtual tea date. Odette, for sending me regular videos of the ocean. Corina, for slowing down to match my pace during XC training, and for teaching me how to wake surf. Jo and Stef, for always being up for an outdoor adventure. Carmen, for sending me a never ending stream of memes to make me smile. Chris, for always joining me for lunch breaks in the quad, regardless of weather. Shawn, for regularly checking in, and taking me on neighbourhood strolls. Rebecca, for always brightening my day.

My success in this program, and life, would not have been possible without the unwavering support from Allana and Alex. Thank you both, for everything. And finally, I would like to thank my partner, Iain, for putting up with all the chaos, and making me laugh every day. I can't wait to plan our next adventure.

Author contributions

This thesis project was conceived by Dr. Laurent Potvin-Trottier. The template used to fabricate the microfluidic master molds was designed by Giselle McCallum. Strain and plasmid construction was completed by Dr. Benjamin Lennart Springstein. The microfabrication, experiment execution and analysis was completed by Krista Jager.

Contents

List of Figures

List of Tables

Chapter 1

Introduction

Information transfer from generation to generation is a fundamental property of biology. Our contemporary understanding of how information is inherited over successive generations is based in genetics and the central dogma of molecular biology: information encoded in genes is heritable[1–3] and flows unidirectionally from nucleic acids to proteins which can be used by an organism to replicate itself[4,5]. However, not everything falls under this powerful unifying concept in biology.

Long before scientists began postulating the central dogma, shepherds all over Europe were dealing with scrapie, a fatal transmissible spongiform encephalopathy (TSE) disease[6]. The etiology of scrapie continued to perplex scientists for decades even as analogous neurodegenerative TSE diseases in humans, such as Creutzfeld-Jakob disease[7,8] and Kuru[9], were identified[10]. Of notable concern to early researchers was the unprecedented appearance of transmission to be both contagious and hereditary[11]. Radio-biologist Tikvah Alper speculated that scrapie must be replicating without nucleic acid after she was unable to determine the genomic size of the causative agent[12]. Her theory that an infectious agent could replicate without nucleic acids was experimentally tested by Stanley Prusiner, leading to his Nobel Prize winning research in which he proposed the term 'prion' to describe proteinaceous infectious particles as the causative agents in TSEs[13].

1.1 The prion hypothesis

Prions can be broadly defined as proteins that are capable of converting between structurally distinct states, of which at least one conformation is self-propagating[14–16]. The prion hypothesis, that a protein conformation can attain different heritable phenotypes without alterations to their encoding genes, falls outside the central dogma of biology and was controversial until spontaneous prion formation *in vitro* and *in vivo* was achieved in the laboratory[17–19].

1.2 Prion structure and strains

Prion proteins can sometimes adopt several structurally distinct self-propagating conformations from the same amino acid sequence[16,20–22]. These genetically identical prion "species" or "strains" vary in their stability and three-dimensional structure[23–27]. Throughout this thesis, we will refer to them as prion "variants" (a terminology commonly used in yeast prions) to avoid confusion with our bacterial strains. Prions typically obtain their self-propagating nature when a soluble native protein undergoes several biochemical steps resulting in amyloid fibrils, which aggregate to form complexes that are capable of nucleating fibril formation in their properly folded counterparts[22,28,28–32]. These amyloid fibril complexes adopt a highly ordered cross-β-structure providing high kinetic and thermodynamic stability from a continuous array of hydrogen bonds[29,33,34]. Although such prions are considered a sub-class of amyloids[35], non-amyloid forming prions have recently been identified, with the specific structure that allows their self-propagation yet to be determined[36].

1.3 Molecular model for prion propagation

The current model for prion propagation is the nucleated polymerization model, in which pre-existing prions act as a template to facilitate the conversion of their properly folded counterparts[37–39]. Complexes of amyloid fibrils are elongated by the addition of newly converted prion monomers, and can be fragmented, sometimes by chaperones such as Hsp104 and ClpB. Fragmentation of these complexes into smaller oligomers, ensures the conversion of more properly folded proteins into the prion fold, creating a self-propagation feedback loop

leading to exponential amplification of the amount of prion proteins (Figure 1.1)[28,37,40–45].

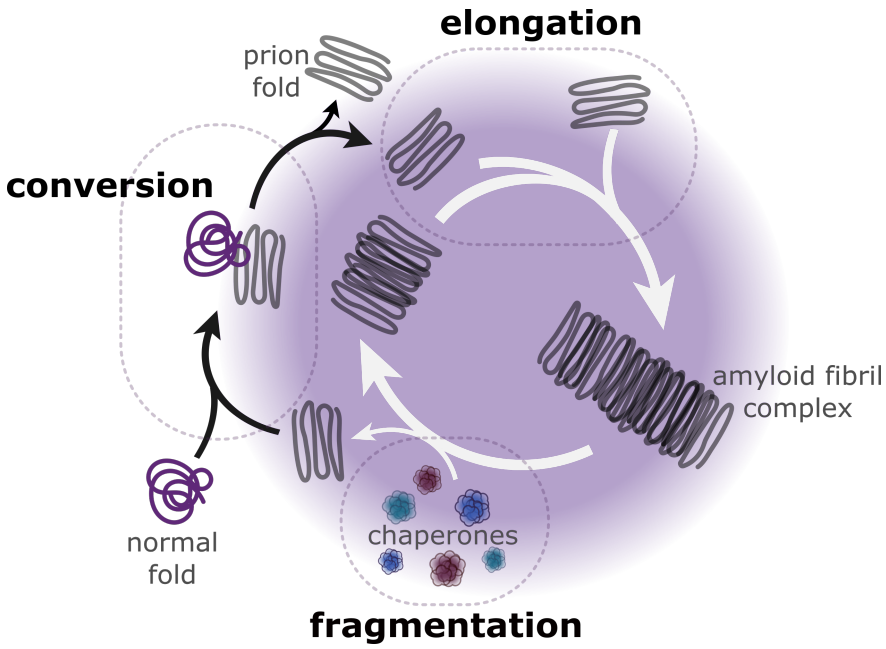

Figure 1.1: Prion propagation follows a cycle of fragmentation and elongation. Fragmentation of amyloid aggregates, sometimes by chaperone machinery such as Hsp104 and ClpB, can provide more oligomers to convert their properly folded counterparts. The addition of monomers to aggregates creates amyloid fibrils. Schematic adapted from Marchante et al.[45] and Scheckel et al.[46]

It also has been suggested that there exists a minimal seed size n below which the aggregates spontaneously return to the native fold, although this seed size remains largely uncharacterized[37]. The balance between elongation and fragmentation enables the stable propagation of prions in a population of dividing cells[47–49].

1.4 Non-pathogenic prions

Although first identified in the context of fatal neurodegenerative disease, non-pathogenic prions have now been found across all domains of life (Table 1), suggesting that they are a common part of biochemical organization and normal cellular function[50–52]. In yeast, transferable prion protein domains (PrDs), which can confer prion properties to the protein it is attached to, have been shown to provide either a loss[53,54] or gain[55] of

function phenotype to the protein, thus acting as a stable epigenetic switch. Therefore, such prions may confer a fitness benefit in fluctuating environments through phenotypic heterogeneity[53,56,57], such as increased resistance to drugs[58] or oxidative stress[57]. These non-pathogenic heritable epigenetic elements in yeast (reviewed by Liebman and Chernoff[59]) also provide a model system for studying prion propagation that has enabled invaluable insights in the pathology of TSE diseases and our overall understanding of prions[60–64].

Table 1.1: Selected non-pathogenic prions and their biological roles. Notation for yeast proteins in their prion state include square brackets and a $^+$ denoting extra-nuclear inheritance and dominance through mating respectively (ex. $[prion^+]$)[60].

Domain	Species	Protein	Normal function	Impact of the prion state
Archaea	*Methanosalsum zhilinae*	CopY family	Transcriptional repressor	Unknown[52]
Bacteria	*Campylobacter hominis*	SSB	Single stranded binding protein	Unknown[65]
Bacteria	*Clostridium botulinum*	Rho	Transcription termination factor	Genome wide transcriptional read-through[51]
Eukarya	*Saccharomyces cerevisiae*	Sup35/$[PSI^+]$	Essential translation release factor	Genome wide translational read-through of stop codons[42]
Eukarya	*Saccharomyces cerevisiae*	Vts1/$[SMAUG^+]$	Developmental regulator	Enables yeast to anticipate nutrient repletion after periods of starvation[66]
Eukarya	*Mus musculus*	CPEB3	Translational repressor	Translational activator involved in long term memory facilitation[67]
Eukarya	*Arabidopsis thaliana*	Luminidependens	Signals flowering in response to temperature change	Unknown[68]

The first identified fungal prion protein, Sup35 of *Saccharomyces cerevisiae*[69–71], served as a model system for yeast prions and has been thoroughly studied. Upon prion conversion, Sup35, denoted $[PSI^+]$ in the prion form, loses its normal function resulting in translational read-through of stop codons[42,50]. The appearance of $[PSI^+]$ is greatly accelerated by the presence of a prion inducibility factor, such as Rnq1 or New1, designated in their prion state as $[PIN^+]$[70,72–74]. However, the mechanisms underlying this interaction have not yet been made clear, with some hypothesizing that $[PIN^+]$ acts as a template for Sup35 prion conversion[31,37,70].

1.4.1 Prions in bacteria

The first example of prion propagation in bacteria was the formation of the *S. cerevisiae* Sup35 prion in *Escherichia coli* cells[75]. The New1 inducibility factor is required for the initial conversion of Sup35 to its prion form, but not for the stable propagation and retention of the Sup35 prion in both *E. coli* and *S. cerevisiae* (Figure 1.2)[43,72,76].

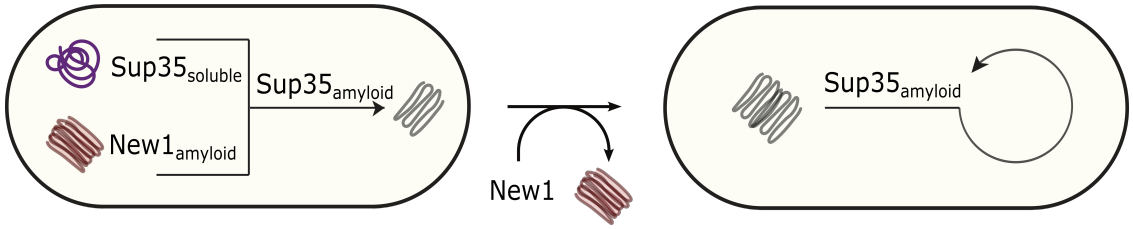

Figure 1.2: Conversion of the yeast Sup35 prion $[PSI^+]$ in *E. coli* bacterial cells is achieved by transient exposure to the New1 $[PIN^+]$ factor[76]. Upon conversion of Sup35 to $[PSI^+]$, the prions will continue to propagate in the absence of New1. Schematic adapted from Yuan et al.[76].

The successful propagation of yeast prions in *E. coli* motivated the search for a bacterial prion. Bioinformatic analysis using an algorithm trained on yeast prion domains[15,77] uncovered thousands of potential candidate prion domains (cPrD) in sequenced bacterial species[51]. Among the cPrDs identified are the transcription termination factor Rho of *Clostridium botulinum* and the single-stranded DNA-binding protein (SSB) from *Campylobacter hominis*[51]. Both *Cb*-Rho and *Ch*-SSB were found to form prions in *E. coli* cells[51,65]. However, the SSB protein relies on the presence of the New1 inducibility factor for initial prion formation[65].

1.4.2 Genetic assay for prion presence and propagation

A lack of tools to detect prion behaviour in bacteria motivated researchers to develop a genetic assay that reports on prion formation and propagation in *E. coli*[65]. This tool makes use of a transcription-based reporter that detects elevated levels of the disaggregase ClpB, as bacterial cells harbouring prions were previously observed to have elevated ClpB expression[65,76]. The promoter for *clpB* (P_{clpB}) is fused to the *lacZ* gene so that an increase in expression consequently results in increased levels of the enzyme β-galactosidase, which can break down a dye-linked substrate called X-gal (5-bromo-4-chloro-indolyl-β-D-galactoside) into an insoluble blue pigment[78–81]. To confirm that blue colonies do indeed contain prions, cell extracts were screened for SDS-stable and SDS-soluble material, as prion aggregates are known to be stable in SDS at room temperature[65,82,83]. With SDS-stable aggregates found only in blue colonies and SDS-soluble aggregates in pale colonies, prion-containing (blue) colonies can be detected based on the colony colour phenotype (Figure 1.3).

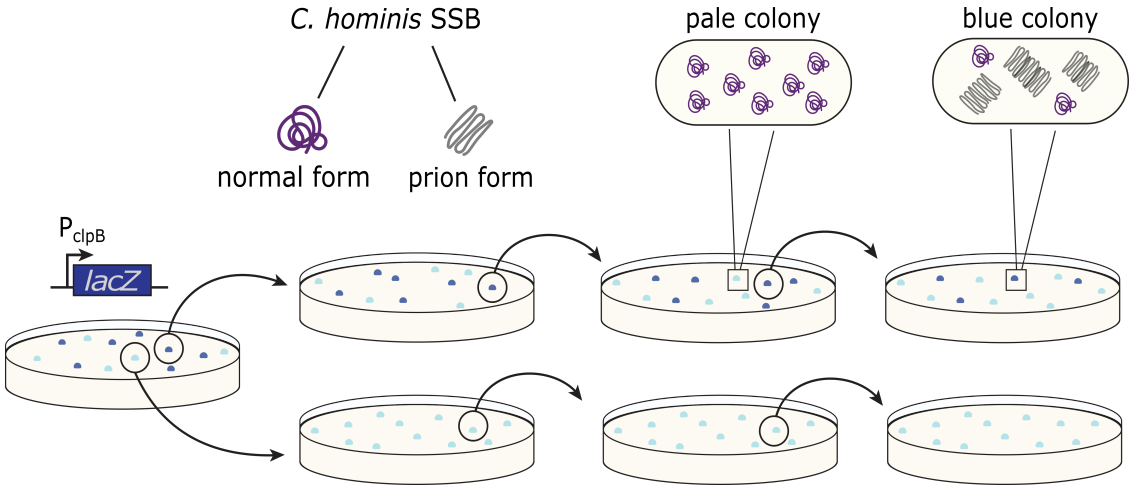

Figure 1.3: Genetic assay for prion detection. Prion-containing *E. coli* colonies can be identified using a P_{clpB}-*lacZ* transcriptional reporter developed by Fleming et al.[65]. Upon plating cell substrate onto X-gal plates, prion colonies are identified by a dark blue colour. Re-plating blue colonies gives rise to plates with a mix of both blue and pale colonies, while re-plating pale colonies give rise to pale colonies only.

Strikingly, this genetic assay showed indefinite propagation of prion-containing cells, yet each re-plating resulted in a small fraction of cells that would spontaneously lose the

prion[65]. Additionally, one lineage produced a higher fraction of prion-containing cells than the others, suggesting that this bacterial prion can adopt unique conformations from the same amino acid sequence (i.e. prion variants), a phenomenon that has previously been observed in yeast and mammalian prion proteins[16,65,84].

1.5 Mechanisms of prion loss in microbes

The extreme rarity of spontaneous transitions between native fold and prion proteins leaves many questions unanswered regarding the underlying molecular mechanisms responsible for their appearance and loss[29,31]. Prion loss (sometimes called "curing") in yeast, i.e. when all prion aggregates are reverted back to their normal fold, has been found to rely on perturbations to the propagation cycle[85], previously depicted in Figure 1.2. This disruption can be achieved by inhibiting fragmentation of prion aggregates[43,49], increasing or decreasing disaggregase activity[43,49], or autophagy[86]. These mechanisms for disrupting the prion propagation cycle in yeast are not mutually exclusive[85]. For example, $[PSI^+]$ has been found to be cured by both inactivation or overproduction of Hsp104, [43]. Inactivation of Hsp104 can disrupt the prion propagation cycle by inhibiting fragmentation, [49] whereas Hsp104 overproduction can cause spontaneous disassembly[47] and asymmetric segregation of prion aggregates to only one of the two progenies[87]. The underlying mechanism of Hsp104 mediated prion curing remains unclear[88–90]. Interestingly, two separate laboratories concluded that heat shock cured weak $[PSI^+]$ variants by asymmetric segregation; however, one lab showed that the daughter cells were cured before the mother cells[91] while the other showed the opposite, with mother cells losing the prion state before the daughters[87]. The difference between these two results has been accounted for by the growth phase of the cells: the transition from log to exponential phase versus exponentially growing cultures respectively[32]. Further investigations of $[PSI^+]$ curing combined with mathematical modelling suggests that in addition to disruptions to the propagation cycle, the oligomeric size of prion aggregates is a crucial contributor to the probability of a loss event occurring[37].

With bacterial prions only recently identified, these previous studies in yeast have raised several questions in bacteria. How are prions lost in *E. coli*? Why do some cells lose the prion state whilst others propagate it indefinitely? Does the currently accepted molecular model for prion propagation in yeast and mammalian cells hold in bacteria? Both the $[PSI^+]$ and the bacterial SSB prion require the presence of ClpB, the Hsp104 bacterial ortholog, to propagate in *E. coli*, suggesting that disaggregase activity is important

for prion propagation[65,76]. However, unlike in wild type (WT) yeast, WT bacterial cells appear to stochastically lose the prion state much more frequently without external stress or perturbations to the propagation cycle[65,76]. It is unclear why prions in bacteria appear to be less stable.

1.6 Single-cell time-lapse microscopy

It is well established that the behaviour of an individual cell within an isogenic population can display broad distributions in cellular processes within a fixed environment[92–95]. This cell-to-cell heterogeneity combined with the stochastic nature of prion inheritance makes it necessary to quantify prion propagation and loss at the single-cell, rather than at the population level.

Single-cell time-lapse microscopy has primarily involved tracking the growth of micro-colonies on agarose pads[96]. Infused with nutrients, agarose pads can support bacterial growth for only a short period of time before cells start competing and forming multiple layers, obstructing single-cell imaging and causing cells to differ in growth rates and metabolic status[97,98]. During these limited generations, the first few are spent adapting to the growing conditions and the latter are spent competing for resources leading to non-steady-state growth conditions, sometimes resulting in non-reproducible quantitative results[98,99]. Additionally, the difference in environments experienced by cells at the edge of the micro-colony compared to those in the center can cause artificial variations in cellular processes, misrepresenting the natural stochasticity and preventing the maintenance of steady-state growth conditions[97–99].

1.6.1 The "mother machine" microfluidic device

The overcrowding limitations associated with agar pads motivated researchers to develop a microfluidic platform, dubbed the "mother machine", to enable long-term imaging of bacterial cells undergoing steady-state growth[100]. This platform traps single bacterial cells in trenches that are perpendicular to a larger feeding channel, thereby allowing single-cell lineages to be followed for hundreds of generations under precisely controlled environmental conditions (Figure 1.4). A constant flow of media through the main channel diffuses into the dead-end cell trenches providing nutrients and flushes away newly divided cells, leaving the

"mother" cell at the top of the cell trench.

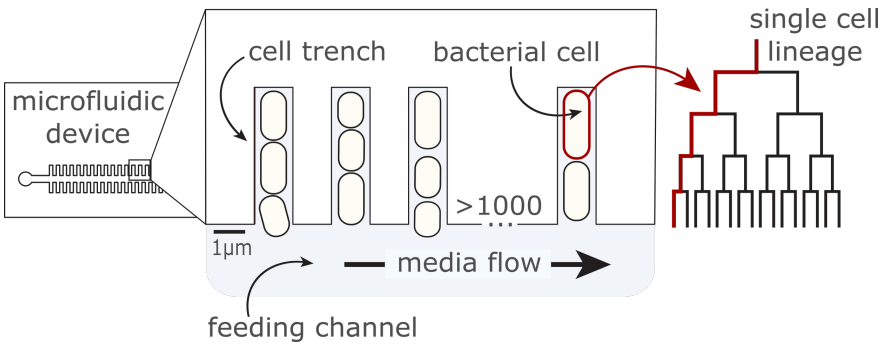

Figure 1.4: The "mother machine" microfluidic device traps individual rod-shaped bacterial cells in dead-end channels perpendicular to a larger feeding channel. As the cells grow and divide the old-pole "mother" cell remains trapped at the end of the cell trench while the newly divided cells are flushed away by constant supply of fresh media, allowing imaging of single cells over hundreds of generations.

1.7 Thesis objectives

The "mother machine" microfluidic device for studying long-term stochastic processes at the single-cell level provides the perfect platform for investigating the propagation and loss of the newly identified bacterial *Ch*-SSB prion. To the best of our knowledge, this will be the first characterization of prion propagation and loss in single bacterial cells. In addition, while some papers have shown time-lapse microscopy over a handful of divisions, they have been limited in the timescale and could not observe loss dynamics under non-perturbed conditions.

In **Chapter 2**, we set up a microfluidic platform for long-term single-cell time-lapse imaging that overcomes the technical challenges of obtaining long time-scale experimental measurements of prion inheritance. **Chapter 3** aims to characterize and quantify prion propagation and loss using the SSB bacterial prion as a model system. We aim to answer three questions:

1. **How is the prion state lost?** In this thesis, we elucidate the molecular mechanism of prion loss in bacteria. We show that prions have two modes of propagation, and that the prion loss is driven by partitioning errors at cell divisions.

2. **Are there variants of bacterial prions?** Previous studies have suggested that variants of bacterial prions could exist, but have not been conclusive. We developed a setup enabling the precise characterization of the dynamic properties of bacterial prions, paving the way for the discovery of prion variants.

3. **What are the general physiological impacts of non-pathogenic prions?** While non-pathogenic prions do not appear to have severe toxicity, it remains unclear how they affect cell physiology. In this thesis, we show that the presence of prions results in a small but significant impact on the growth rate. However, our preliminary results indicate that they could also provide protection against proteotoxic stress.

Chapter 2

A microfluidic platform for single-cell time-lapse imaging

2.1 Introduction

Microfluidics focuses on the precise manipulation of fluid in systems with at least one dimension in the range of 100nm to 100µm[101–103]. The field is fundamentally multidisciplinary, and relies heavily on engineering and physics principles to create the microsystems in which these fluids are manipulated. The desire to measure single-cell dynamics within a microfluidic device has driven the development of specific platforms, often uniquely designed for each application. These platforms have been used in many ways, such as quantifying complex growth[100,104,105] and gene expression dynamics[106–109], as well as investigating host-pathogen interactions[110], antibiotic tolerance[111], quorum sensing[112], and bacterial interactions[113].

The microfluidic devices used throughout this thesis, modelled after the "mother machine"[100], have their features cast into polydimethylsiloxane (PDMS), commonly used for its permeability to oxygen, chemical and thermal stability, biocompatibility and optical transparency[114]. The embedded microstructures in the PDMS leave a gap when plasma-bound to a glass coverslip creating space for the cells and media (Figure 2.1a). Media is pumped through the inlet into the main feeding channel and then exits through the outlet into a waste beaker (Figure 2.1b). The lineages of growing cells in the trenches can then be followed under precisely controlled environmental conditions using time-lapse microscopy.

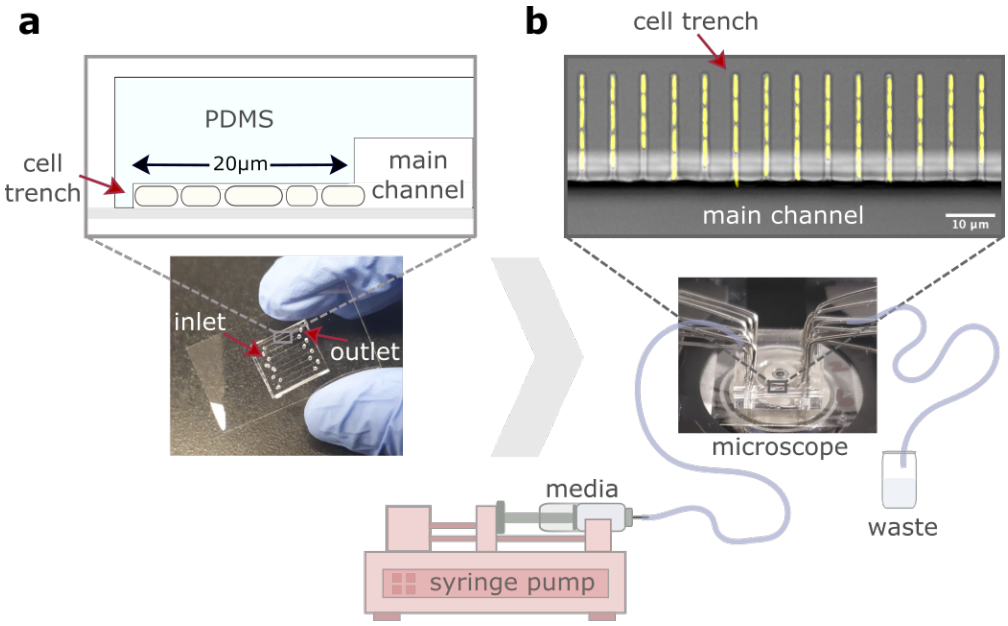

Figure 2.1: A complete microfluidic device. a) a side-view of a microfluidic device with the microfluidic features embedded into PDMS. The chip is bonded to a coverglass for microscopy, closing the channels. b) A top-down view of a microfluidic device loaded with bacterial cells. Media is pumped through the completed device to feed the cells (yellow) during a time-lapse microscopy experiment

In order to measure single-cell dynamics over long time scales, a microfluidic device with the proper dimensions is required to prevent the cells from being flushed out, and to replicate the growth rate and physiology observed in liquid culture[98]. We therefore built a library of molds to create microfluidic devices of varying dimensions that can accommodate different bacterial species and strains. This chapter will describe the methods and challenges of fabricating these devices.

2.2 Microfabrication

2.2.1 Device design

When scaling down from the macro- to microscale the behaviour of the flow of fluids transitions from having a dominant inertial force to a dominant viscous force effect[115]. The ratio of the inertial to viscous forces is referred to as the Reynolds number (Re)[116]:

$$Re = \frac{\text{(inertial forces)}}{\text{(viscous forces)}} = \frac{\rho \nu L}{\upsilon}$$

where the density (kg/m^3) of the fluid ρ, the kinematic velocity (m/s) of the flow ν, and the characteristic linear dimension L are the inertial forces, and the dynamic viscosity (mPa·s) is represented by υ. Typical flow regimes, such as those found in household pipes, have a high Reynolds number (>4000) resulting in unstable and turbulent flow (Figure 2.2). As the Reynolds number falls (<2000), the flow regime becomes stable and laminar, with diffusion acting as the only method of mixing[117,118]. The laminar flow regime therefore provides challenges for channel microfluidic devices, as nutrients within the medium depend on diffusion to enter the cell trenches and for waste metabolites to be flushed away.

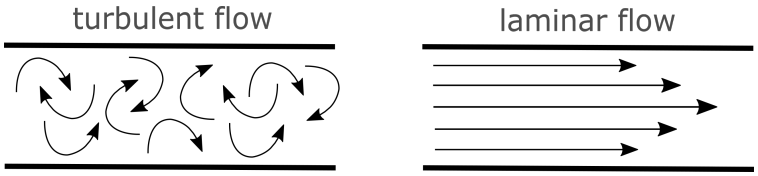

Figure 2.2: Turbulent flow (left) stable laminar flow (right) in a channel. The black arrows indicate the direction of the flow. Adapted from Fallahi et al.[119].

All of the microfluidic devices used throughout this thesis have dimensions that fit well within the laminar flow regime. As diffusion is the only method of mixing at this scale, the length of the cell trenches determines how variable the feeding is for cells along the trench (i.e. cells further away from the trench opening go longer before receiving fresh medium)[99,120]. The original mother machine microfluidic device contained cell trenches with a length of 30 µm[100]. As recent work has found growth-limiting effects associated with cell trenches >20 µm long[98], the devices used throughout this thesis were modified to have a cell trench length of 20 µm, ensuring uniform feeding along the trench. Due to the variation in sizes of bacterial species and strains, our template contains devices with four different cell trench widths ranging from 1.1 µm to 1.7 µm (Figure 2.3b).

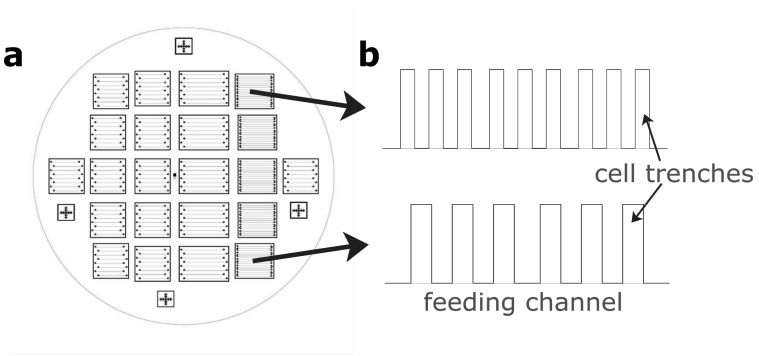

Figure 2.3: Varying dimensions of the microfluidic device template. a) The template used to create the molds for fabricating the microfluidic devices in this thesis with b) varying cell trench widths to accommodate a variety of bacterial species and strains.

If the dimensions are too narrow, cells cannot easily enter a trench, with those that do enter exhibiting reduced growth and affected cell morphology[98]. Trenches that are too tall enable the bacteria to grow on top of one another, making post-experiment segmentation difficult (Figure 2.4a).

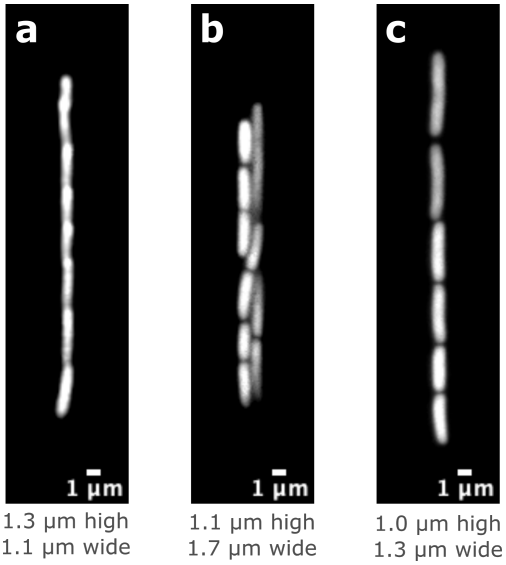

Figure 2.4: Importance of a precise cell trench size to ensure the bacterial cells are healthy and the images taken during an experiment can be analysed. Fluorescence microscopy images of *E. coli* cells within microfluidic devices of varying dimensions. Cell trenches that are a) too high result in cells growing over top of one-another, b) too wide result in cells growing side-by-side, c) slightly wider than the height dimension produces segmentable images.

Additionally, trenches that are too wide result in cells growing side-by-side, which adds additional challenges to post-experiment analysis (Figure 2.4b). Thus, the precise fit required for healthy cell growth and usable data typically involves width dimensions greater than the height, but shy of allowing side-by-side growth (Figure 2.4c). With the width of the cell trenches already established in the template design, the height is determined during the photolithography process described in the following section.

2.2.2 Photolithography

Photolithography is the process of transferring a design from a template (photomask) onto the light sensitive photoresist material coating a surface, which acts as a mold for the finalized microfluidic device[114,121,122]. To create the microstructures that will serve as a template for the finalized microfluidic devices used in this thesis, the molds used throughout this thesis were fabricated following standard photolithography practices at the McGill Nanotools microfabrication facility (Montréal, Canada), a class 100 cleanroom, to reduce particulate contamination.

Molds are built up layer-by-layer to create features of different sizes. Starting with a silicon wafer as a base surface, the first layer of negative photoresist[123] is deposited, which will become the cell trenches. As the negative photoresist is light sensitive, an ultraviolet (UV) light is shone through the template cross-linking the exposed areas. The rest of the photoresist is washed away leaving the desired features on the wafer (Figure 2.5a). A detailed protocol for the fabrication process is described in Chapter 5: Materials and Methods (section 5.1.1). This process is repeated a second time with the addition of an alignment step to create the larger feeding channels required for our devices. The higher feeding channel ensures that the hydraulic resistance of the channel is relatively low and that media can be pumped through via syringe pumps. A challenging process in the manufacturing of the mold is ensuring the precise alignment of these consecutive layers. The slightest variation in the x, y, z, or rotational axis can result in mis-alignment of the cell trenches with the feeding channel, rendering the mold useless (Figure 2.5b).

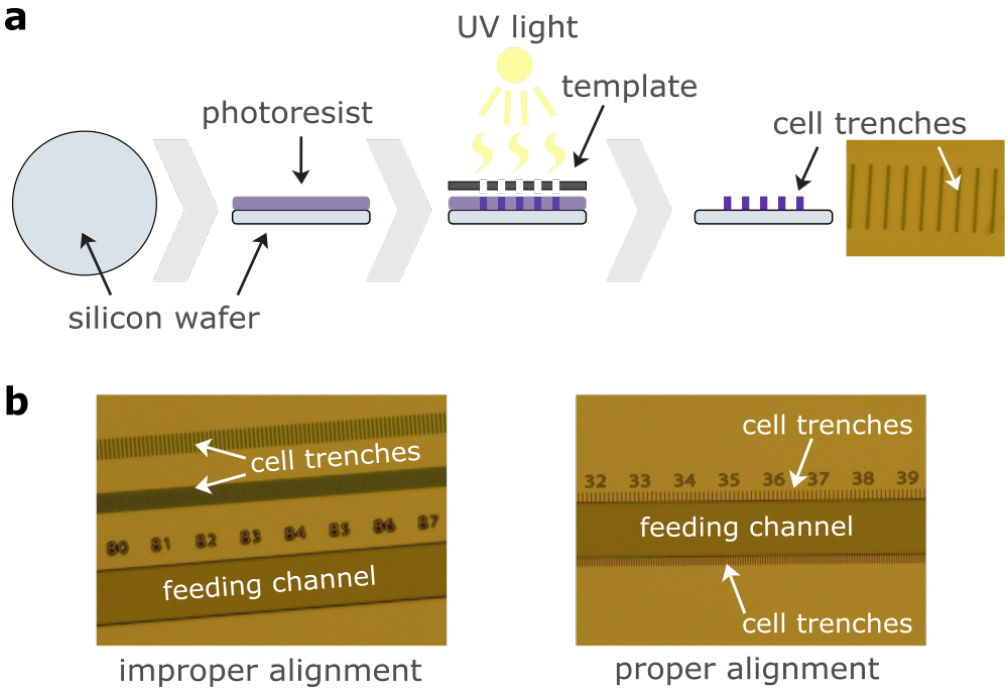

Figure 2.5: Brief photolithography workflow with alignment examples. a) Photoresist is deposited onto a silicon wafer. The areas of negative photoresist exposed to UV light though the template become cross-linked and permanently adhere to the silicon wafer. b) Microscopy images of the second layer with an example of improper alignment of the two layers on the left, resulting in the cell trenches not connected to the feeding channel. The image on the right shows proper alignment.

Alignment markers are included in the template designs to reduce these errors. However, depending on the design of the markers and the equipment available to align the layers, simply having these markers is not enough to ensure proper alignment, as seen in Figure 2.5b. In order to reduce the errors and time allocated to photomask alignment, the markers used to fabricate the molds used in this thesis were re-designed for future fabrication based on experience with the equipment available at the McGill Nanotools facility. The initial alignment marker design consists of several plus signs arranged in a larger formation that are built into the first layer on the wafer. The second layer consists of boxes, or windows, used to align the plus signs into (Figure 2.6a). The improved design includes additional boxes, and arrows acting as a landing strip to reduce the time required to locate the markers (Figure 2.6b).

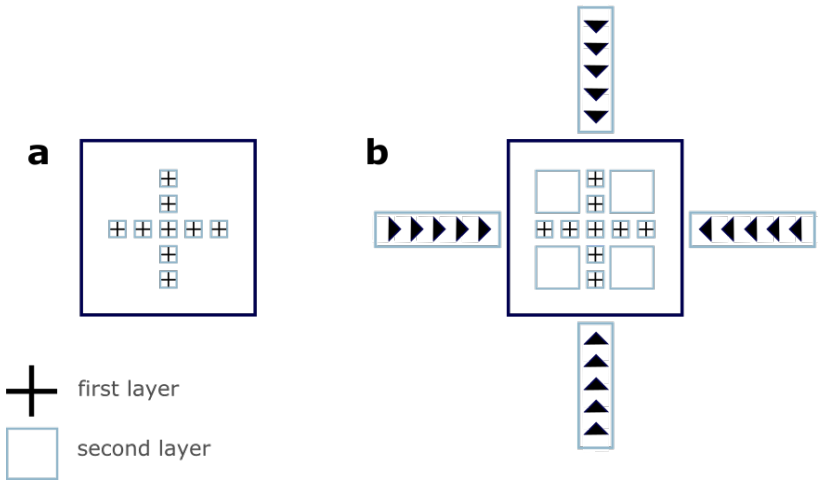

Figure 2.6: Template alignment marker improvements. The second layer (blue) is used to align the first layer (black) during the photolithography process. a) shows the original alignment markers used for the wafers produced for this thesis, and b) demonstrates improvements on the design that will be used for future wafer fabrication.

2.3 Library of microfluidic molds

Once fabricated, the silicon wafers bearing our device design can be used as a master mold almost indefinitely. As previously mentioned, bacterial strains vary in size. To accommodate the range of bacterial strains used in our laboratory, several molds with cell trench heights varying from 0.9 µm to 1.3 µm by 0.1 µm increments were fabricated. The cell trench heights can be matched with the variation of cell trench widths to create an ideal fit. The strains listed in Table 2.1 have been successfully tested with our molds.

Table 2.1: Bacterial lab strains and the corresponding cell trench heights of the microfluidic devices they fit in.

Cell trench height	Bacterial strain
1.0 µm	*Rhodobacter capsulatus*
	Bacteroides thetaiotaomicron
	Escherichia coli MG1655
1.1 µm	*Escherichia coli* DH5alphaZ1
1.3 µm	*Escherichia coli* MC4100

The *E.coli* MG1655 strains used throughout this thesis grow well in the 1.0 µm tall and either the 1.1 µm or 1.3 µm wide devices, as both widths allow media to diffuse in but are not so wide that cells are able to grow side-by-side. The devices used in the following chapter are 1.0 µm tall and 1.3 µm wide unless otherwise specified. Figure 2.7a shows a representative example of an *E. coli* MG1655 strain loaded into a completed device. The "mother" cell in each individual cell trench is followed for the duration of an experiment (Figure 2.7b), with the cells growing and dividing consistently over time (Figure 2.7c-d).

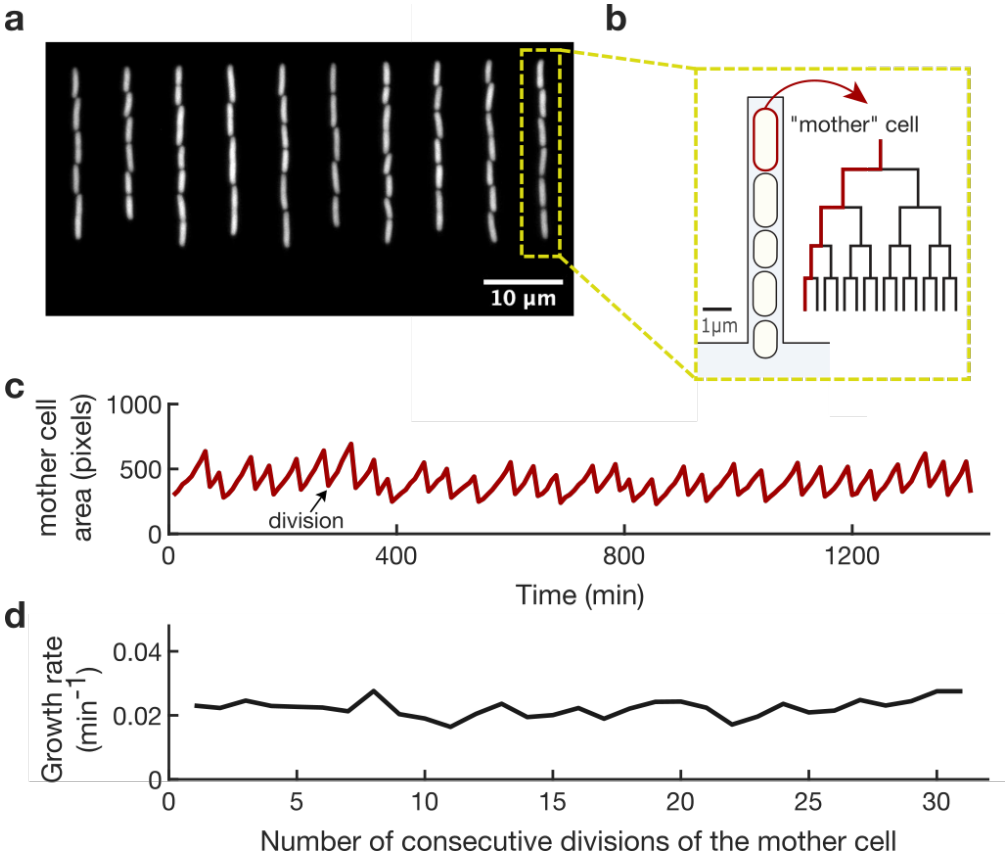

Figure 2.7: Representative *E. coli* MG1655 strain growing in our microfluidic device. a) A microscopy snapshot of a partial field of view during an experiment showing 10 cell trenches filled with *E. coli* cells. b) Schematic representation of an individual cell trench, in which the mother cell is tracked. c) An example time trace showing the area of the mother cell over time with d) consistent growth rate during each consecutive division. Cell division occurs every $\sim$ 50 minutes at 30°C, same as found in other microfluidic platforms[105] and in culture tubes outside the device.

Chapter 3

Single-cell dynamics of bacterial prions

3.1 Introduction

As prions have only recently been discovered in bacteria[51,65], their kinetics and loss mechanisms have yet to be determined. With our microfluidic platform for time-lapse single-cell imaging, we set out to quantify and characterize the *Campylobacter hominis* SSB (*Ch*-SSB) prion loss at the single-cell level. We elucidate the molecular mechanism for prion loss and two different modes of propagation. Using our platform, we also investigated if SSB prion domains from different bacterial species have the same loss kinetics and mechanisms. This chapter will also provide preliminary evidence on the existence of bacterial prion variants, i.e. different prion conformations with varying stability from the same amino acid sequence, a phenomenon previously observed in yeast[16] and mammalian cell prions[124]. Finally, we investigated if the SSB prion confers a burden onto the cells that harbour them, and whether this provides them with increased resistance to proteotoxic stress.

3.1.1 Visualization of protein aggregates

In order to characterize prion propagation, it was first necessary to induce the prion state and distinguish cells with normal protein conformations from cells harbouring prions. To do this, *Ch*-SSB PrD and the New1 initiation factor were fused to mEYFP (mEFYP-SSB PrD) and mScarlet (New1-mScarlet), respectively, enabling prion aggregates to be detected using fluorescence microscopy through aggregated/non-diffuse fluorescent

signal (Supplementary Figure 6.1, Figure 3.1). New1 is required for the conversion of *Ch*-SSB to its prion form, but not for stable *Ch*-SSB propagation[65]. Therefore, to induce the formation of the prion and monitor its propagation, New1 was transiently expressed. This was possible due to the temperature sensitive origin of replication of the plasmid containing New1. After *Ch*-SSB prion conversion, we confirmed New1 loss with antibiotic sensitivity and the absence of red fluorescence (Supplementary Figure 6.2). Additionally, we used the genetic assay developed by Fleming et al.[65] to identify colonies containing *Ch*-SSB prions (Figure 3.1). Consistent with observations by Fleming et al.[65], pale colonies (prion-negative) give rise to 100% pale colonies, whereas blue colonies (prion-positive) give rise to a mix of both (Figure 3.1).

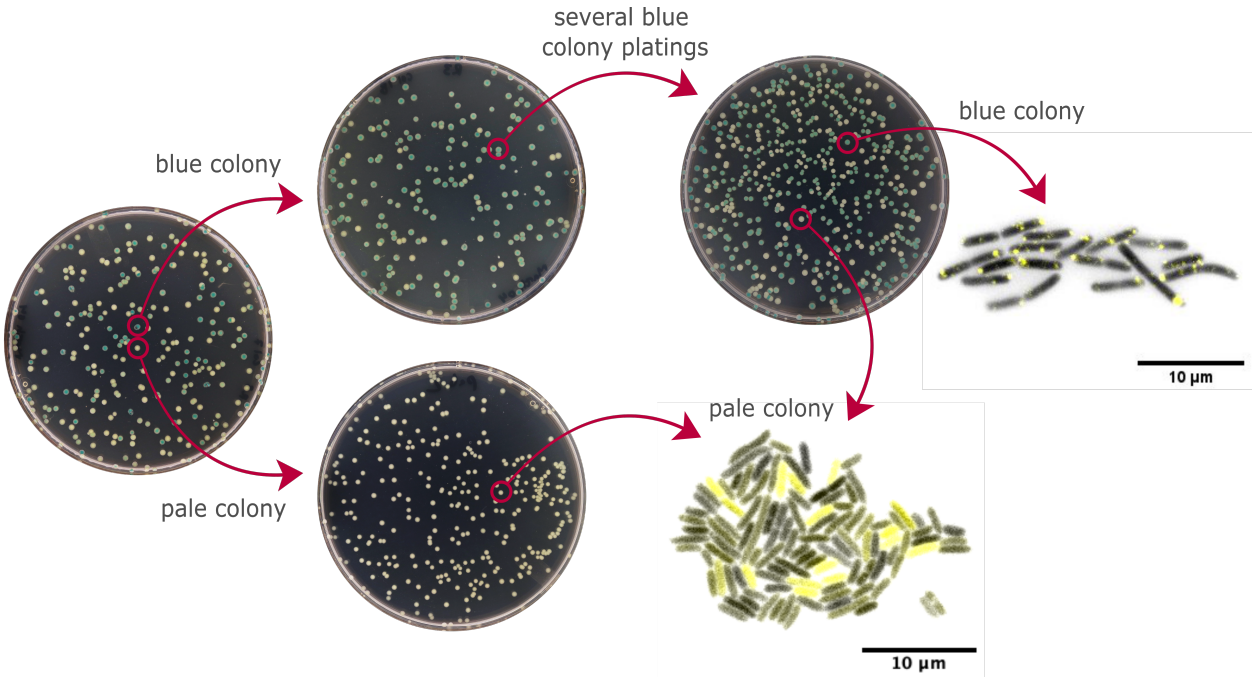

Figure 3.1: Plating assay for detecting the presence of prions at the colony level. Re-plating experiments with strain KLJ15 using an assay to detect prion propagation show that once lost, cells do not regain the prion state: pale (prion-negative) colonies give rise to only pale colonies. On the other hand, blue (prion-positive) colonies give rise to a mix of both. Microscopy images of *E. coli* were taken on an agarose pad, with diffuse YFP fluorescence observed in the cells from the pale colony, and aggregated YFP fluorescence (yellow spots) in the cells from the blue colony.

3.1.2 Confirmation that visualized aggregates are prions

Prions can be distinguished from their normal conformation by running cell lysates on semi denaturing detergent agarose gel electrophoresis (SDD-AGE)[82]. To confirm that the visualized aggregates were prions, cell lysates from our constructs for SDD-AGE were prepared as described in Fleming et al.[65] by Dr. Benjamin Springstein. A Western Blot confirms that all selected blue colonies contain SDS-insoluble *Ch*-SSB aggregates whereas pale colonies contain only soluble *Ch*-SSB proteins (Supplementary Figure 6.3). Additionally, because aggregated fluorescence (i.e. fluorescence not uniformly diffuse throughout the cells) was only present in the blue colonies, we concluded that cells containing aggregated YFP-PrD represented cells with prions.

3.1.3 Overview of experimental setup

For the following experiments, prion-containing colonies were grown in liquid culture and loaded into a microfluidic device for single-cell time-lapse imaging. Figure 3.2 shows an overview of this experimental setup. Once a time-lapse microscopy experiment is complete, an automated image segmentation platform creates a continuous time trace for each individual cell and identifies prion aggregates as fluorescent spots. More detail on this methodology is available in Chapter 5.

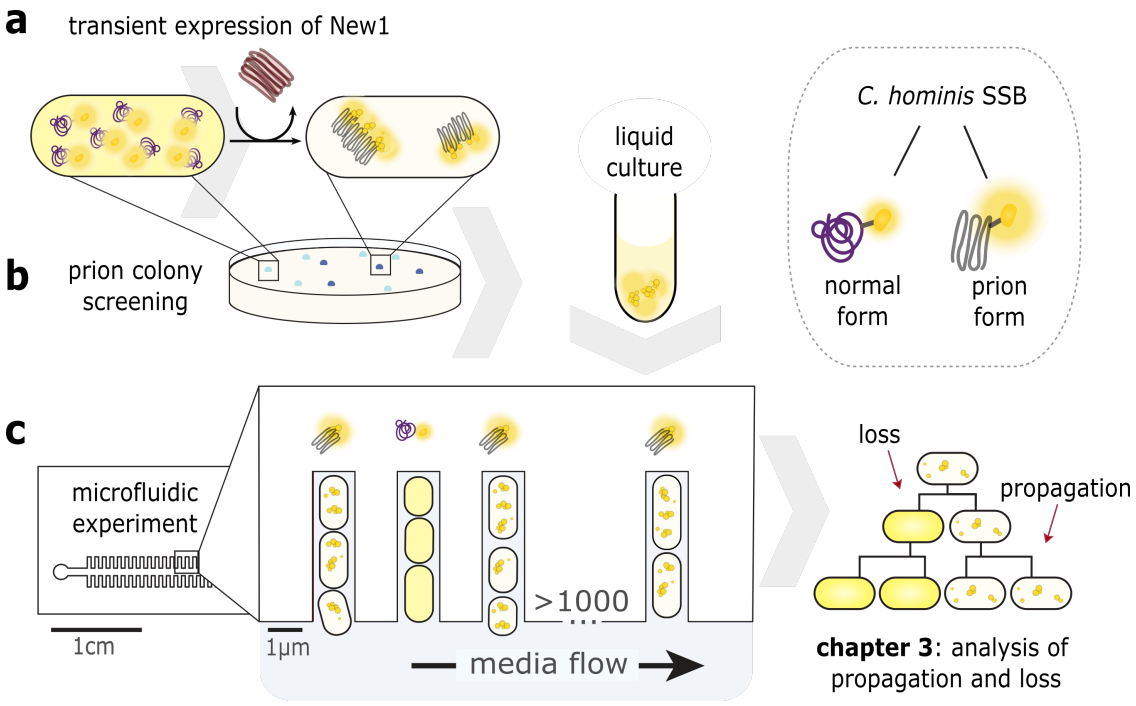

Figure 3.2: An overview of the experimental setup for quantifying prion propagation and loss. a) Cultures that have been cured of New1 give rise to both pale and blue colonies. b) Prion-containing colonies (blue) are grown up in liquid culture and screened for prion content prior to loading in a microfluidic device. c) Epifluorescent time-lapse imaging follows thousands of single cells for 1-3 days as they grow and divide in the device.

3.2 Prion loss is kinetics

Prion loss is determined when a cell continues to produce YFP fluorescence, but no longer forms aggregated foci. By displaying images of a single cell side-by-side over time as a kymograph with the colour scale emphasizing aggregates, we can clearly see loss events occurring as the cells grow and divide (Figure 3.3a). We used a spot-finding algorithm that identifies cells harbouring prions for each individual cell trace and determines the timing of loss events (Figure 3.3b, Chapter 5 section 5.3.2). This analysis was consistent in time, where cells that lost prions did not reform them, but continued to produce diffuse YFP fluorescence.

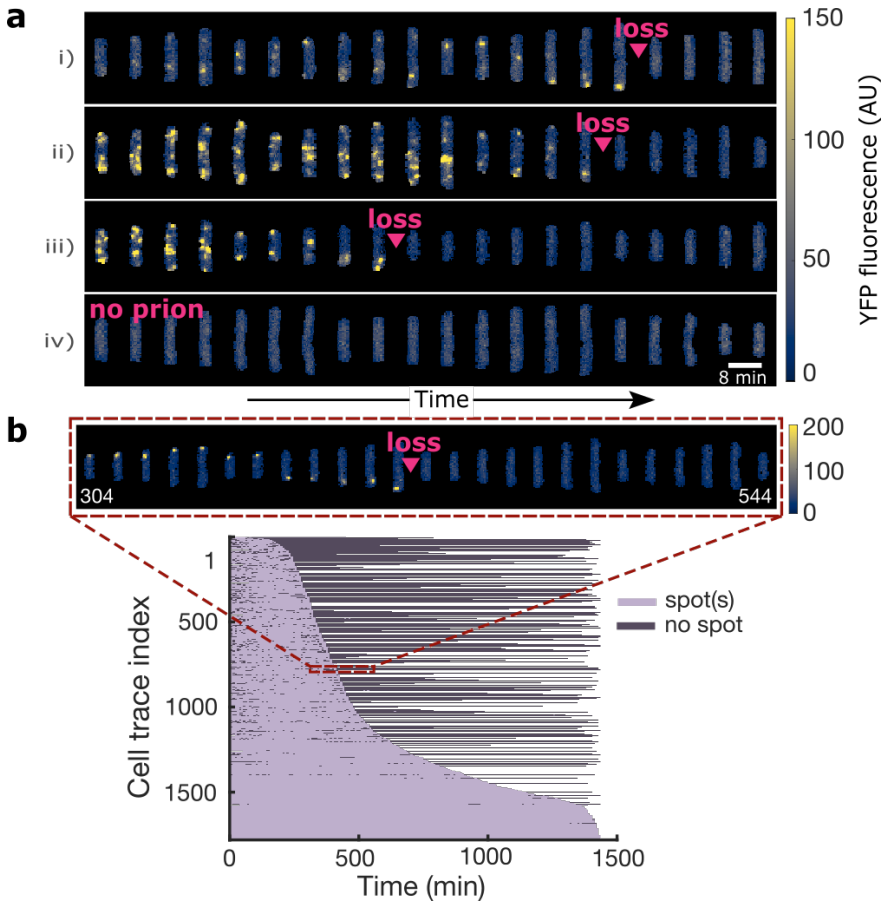

Figure 3.3: A spot-finding algorithm identifies cells in the prion state. a) The first three kymographs show prion loss events identified at a time point shown by a pink triangle. The fourth trace shows a cell that did not have the prion when it was loaded into our microfluidic device. Note that the contrast here emphasizes the aggregates, and that for all these traces the overall concentration of fluorescence is constant (i.e. fluorescence is produced at the same level after loss of the prion, see e.g. Figure 3.7). b) All cell traces sorted by the time they lost the prion state. Each trace is colour coded showing the presence (purple) and absence (grey) of spots. Above the plot is an example cell (trace index 734) that loses the prion at 400 minutes with its associated kymograph from 304 to 544 minutes. All images were taken 8 minutes apart.

By quantifying prion loss, we can determine if it is memoryless, i.e. independent of time spent in the state. The only continuous distribution with a memoryless property is the exponential distribution[125]. We can therefore plot the cumulative distribution of cells losing the prion state and determine if it follows the memoryless distribution. The probability that a cell propagates a prion for more than t time is the survival function (1 - the cumulative distribution function):

$$\text{Cumulative distribution function (CDF): } F(t) = P(T \leq t)$$

$$\text{Survival function (1-CDF): } S(t) = P(T > t) = 1 - F(t) \text{ for } t > 0$$

where T is the length of time the prion is propagated. Initially, we assumed that all prion-containing cells in a clonal population would have similar loss kinetics. Plotting the fraction of cells in the prion state as a function of time (1-CDF) revealed a biphasic distribution, where the rate of prion loss starts off rapidly and then slows down over time (Figure 3.4a). This suggests that there could be distinct subpopulations of cells with different loss kinetics. Visual inspection of prion containing cells revealed two prion aggregate phenotypes. In one subpopulation, a single large aggregate was present, typically located at the pole closest to the end of the cell trench, i.e. the old-pole, which is not renewed after cell division. In the other subpopulation, several small aggregates were dispersed throughout the cell (Figure 3.4b). The old-pole subpopulation continuously gave rise to progeny with the small aggregate phenotype, indicating that these cells indeed contained prions rather than other non-specific protein aggregates (Figure 3.4c).

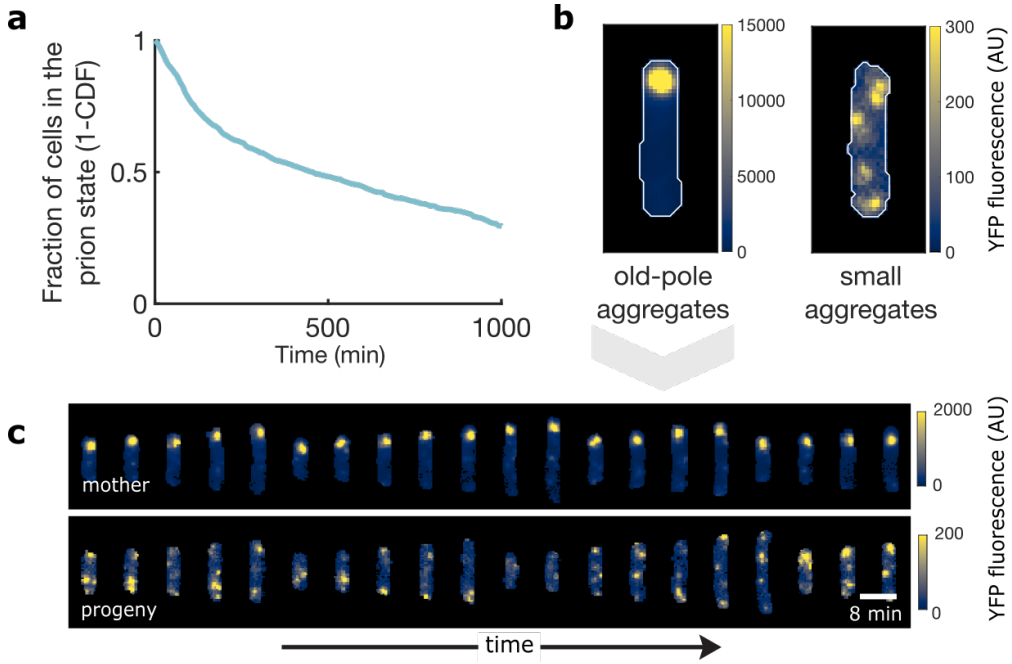

Figure 3.4: The fraction of cells in the prion state over time (1-CDF) for all aggregate phenotypes shows a biphasic decay (n=1,779 cells followed). b) Cells typically either have one large prion aggregate located at the old-pole, or several smaller aggregates dispersed throughout the cell. c) Kymograph showing the "mother" cell with an old-pole aggregate (located at the top of the cell) and the progeny with many small aggregates. Images were taken 8 minutes apart.

As the old-pole aggregates were substantially brighter than the small aggregates (Figure 3.4b), the two subpopulations can be separated using the median top 10% of YFP pixel values in the cell image divided by the YFP protein concentration for the entire cell. We refer to this as the peak over average ratio. While there was incomplete separation, a threshold value of 5 adequately separated the phenotypes after manual inspection (Figure 3.5). Cells with a peak over average fluorescence value below 5 were considered to have small aggregates.

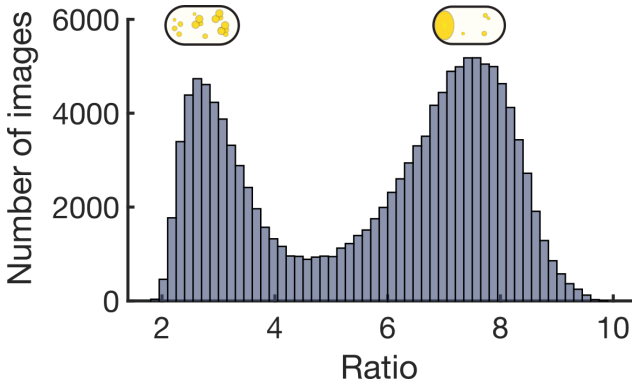

Figure 3.5: Prion phenotype identification. Histogram showing the ratio of peak YFP over average YFP fluorescence for all images of prion containing cells (n = 130,560)

Separating the two sub-populations based on prion aggregate phenotype revealed that the two subpopulations had drastically different loss distributions (Figure 3.4). The loss kinetics of the prion state in cells harbouring several small prion aggregates follows an exponential decay (R^2=0.998) indicating that prion loss is a memoryless process for this group (Figure 3.6a). The half-life of the prion state ($t_{1/2}$), measured as the time it takes for half of the prion-containing cells to lose the prion (1-CDF = 0.5), is ∼2 cell generations (96 minutes). In contrast, the large old-pole aggregates rarely lose the prion state, displaying stable long-term propagation (Figure 3.6b).

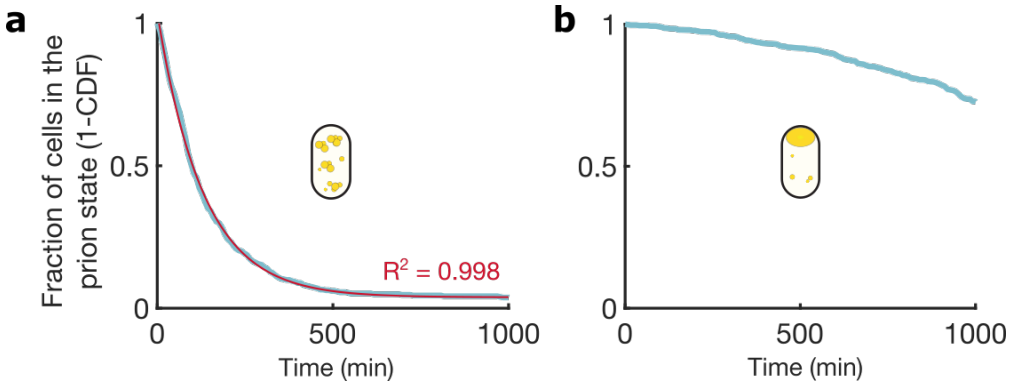

Figure 3.6: The fraction of cells in the prion state over time (1-CDF) separated based on aggregate phenotype. Splitting the population of prion containing cells into two groups reveals distinct loss kinetics. a) The small aggregate group (n=1,014 cells followed) follows an exponential distribution (red line) with an R^2=0.998. b) The old-pole phenotype (n=765 cells followed) rarely experiences a loss event.

Cells harbouring the old-pole aggregates typically maintained the prion state for the duration of an experiment, generating small-aggregates containing progeny cells at division. The old-pole aggregates were mostly immobile, presumably due to their size preventing movement past the nucleoid. On rare occasions, the large aggregate was able to move away from the old-pole and was inherited by its progeny, resulting in prion loss in the mother cell. These data suggest two modes of bacterial prion propagation. The small aggregates were relatively unstable and their loss followed exponential decay. Contrastingly, cells containing the old-pole aggregates were very stable and divided asymmetrically, generating one cell containing small aggregates and one old-pole aggregate containing cell. In our device, as we only track the mother/old-pole cells, this phenotype is highly enriched. In an exponentially growing culture, the old-pole cell would represent an exponentially diminishing subpopulation, yet would be capable of preserving the prion state for long periods of time. In the future, it would be interesting to confirm the presence of this subpopulation using alternative reporters for the prion state that do not depend on a fluorescent protein translation fusion, as we cannot exclude the possibility that the formation of these large aggregates is influenced by the presence of the fluorescent protein[126]. As cells with the old-pole aggregates display vastly different loss kinetics than cells with small aggregates, the following analyses focus solely on cells with the small aggregate phenotype.

3.3 Prion loss is driven by partitioning errors at cell division

It was previously found that Sup35 prion loss events in *E. coli* cells were correlated with a drop in Sup35 protein levels[76]. This motivated our first hypothesis: stochastic fluctuations resulting in under-expression of the *Ch*-SSB protein causes loss events. To determine if *Ch*-SSB prion loss events are also correlated with a drop in protein levels, we plotted the concentration of YFP, i.e. the expression of the SSB protein, leading up to a loss event. Unlike with the Sup35 prion, there appeared to be no drop in *Ch*-SSB protein levels prior to the loss event (Figure 3.7).

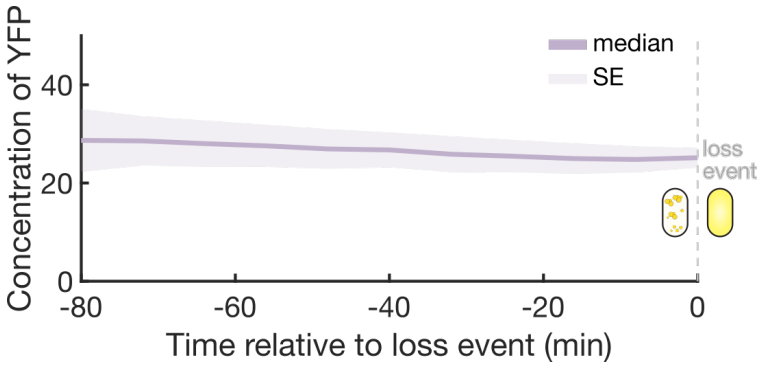

Figure 3.7: The expression of the SSB protein is constant before the prion loss event. Traces were aligned at the moment of prion loss, and the median concentration of YFP (i.e. total YFP/cell area) over time is shown relative to the loss event (purple, n=893) with the standard error of the mean (SE) as the envelope. The loss event is indicated with a dotted grey line at time=0.

With *Ch*-SSB protein levels remaining steady leading up to a loss event, we explored a second hypothesis: partitioning errors drive prion loss events. Partitioning errors occur from the stochastic division of molecules between the mother and progeny cells during division[127]. We previously observed that asymmetric segregation of aggregates can cause prion loss events within the old-pole sub-population. As partitioning errors occur during division, to test our hypothesis with the small aggregate sub-population, we first wanted to see if prion loss events were correlated with cellular division. Determining the cell cycle position at the time of prion loss revealed that most cells lost the prion state right after cell division (77% lost at division, n=893 prion losses) (Figure 3.6a). To further confirm that the stochastic partitioning of prion aggregates at the time of division causes prion loss, we quantified the partitioning error (Q) of prions as the difference in total YFP (i.e. protein abundance) between the mother and progeny cells immediately following cell division (Figure 3.6b):

$$Q = \frac{\text{(YFP mother cell - YFP progeny cell)}}{\text{(YFP progeny cell + YFP mother cell)}}$$

If there is an equal amount of YFP proteins in both the mother and progeny cells immediately following cell division, the partitioning error will equal zero. Q will be a positive number if mother cells contain more YFP than their progeny cells, and a negative number if more YFP are present in the progeny cells after division.

For cells that lost the prion state at division (77%, n=893 total cells), right at the time of loss there is a large negative partitioning error, showing the transfer of YFP proteins to the progeny cells (Figure 3.8c). Of these progeny cells, 89% (n=886 total progeny cells) continue to propagate the prion state for at least one cell cycle (∼6 images) after a loss event in the mother cell (Figure 3.8d). This suggests that instead of being simply "lost", prion aggregates are transferred into that progeny cell through random segregation. For the cells with prion loss events not occurring at cell division (23%, n=893 total cells), they appeared to have a large partitioning error into the progeny cell just prior to their loss, suggesting that partitioning errors also play a role in these cells (Figure 3.8c).

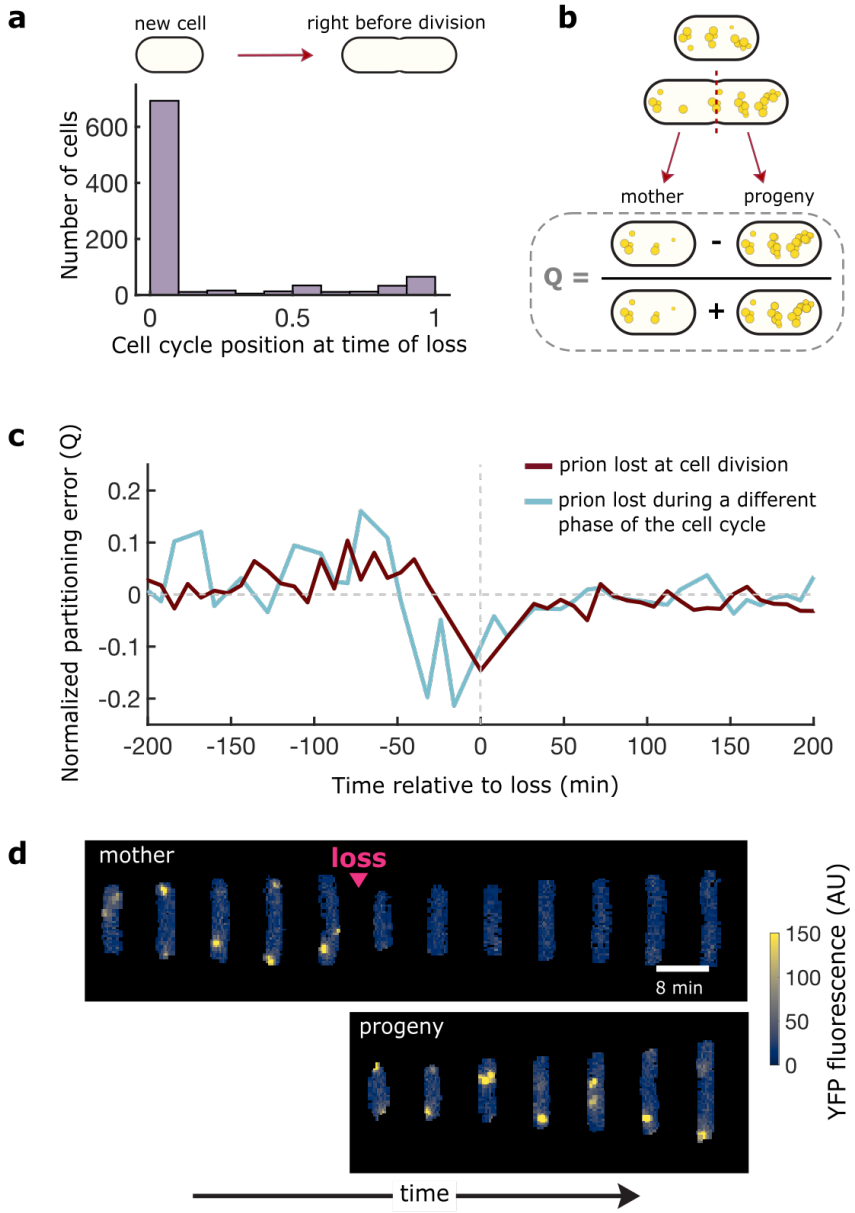

Figure 3.8: Prion loss is driven by partitioning errors at cell division. a) The majority of cells (77%, n=692/893) lose the prion right after cell division, indicated as the cell cycle position zero in the histogram. b) Schematic representation of the partitioning error (Q) calculation. c) The median partitioning error (normalized for protein concentration) of cells that lost the prion state at cell division (red line, n=692) and cells that lost the prion state during a different phase of the cell cycle (blue line, n=201). The median was calculated using cell traces that had more than 10 cell divisions occur at a single time point (n=893 cell traces). d) Kymograph example of a mother cell losing the prion at cell division (pink triangle) and the progeny cell (below) continuing to harbour prions. Images were taken 8 minutes apart.

Taken together, these results suggest that the prion loss is caused by partitioning of aggregates to the daughter cell, prior or at the moment of prion loss, and that the prion continues to be propagated in that daughter cell for the limited time where we can track it. Therefore, we conclude that *Ch*-SSB prion loss is driven by partitioning errors. This suggests that the distribution of aggregate size is crucial for the stability of the prion, as larger aggregates would result in larger partitioning errors.

3.4 Characterization of orthologous SSB PrDs

In addition to the *Ch*-SSB PrD[65], our collaborator Dr. Ann Hochschild's group (Dept. of Microbiology, Harvard Medical School) has identified SSB PrDs from other bacterial species that can form prions in *E. coli* (unpublished). To provide further support that prion loss in bacteria is a memoryless process driven by partitioning errors, we investigated orthologous SSBs from different bacterial species to see if they have the same properties as the *Ch*-SSB prion. Dr. Hochschild's group also performed random mutagenesis of the *Ch*-SSB PrD and discovered a mutant that is able to spontaneously form aggregates without the presence of New1, hereafter referred to as Ch_{mut}. It remains unclear if this mutant is a prion forming protein or simply a protein that aggregates at high concentration.

The mutant and SSB PrDs from *Lactobacillus heilongjiangensis* (*Lh*-SSB) and *Moraxella lincolnii* (*Ml*-SSB) were grown in our microfluidic devices following the previous experimental workflow used with *Ch*-SSB. Focusing our analysis again on cells with small aggregates, we found that the fraction of cells in the prion state over time for *Lh*-SSB, *Ml*-SSB, and Ch_{mut} all follow an exponential decay, however the $t_{1/2}$ of the prion state varied dramatically, increasing from ∼2 generations in *Ch*-SSB to a remarkable ∼18 generations in *Ml*-SSB (Figure 3.9a). The majority of loss events occurred at cell division for all of the orthologs and Ch_{mut} (Figure 3.9b). Additionally, as seen previously with *Ch*-SSB, the mutant and orthologs all have larger partitioning errors prior to prion loss, with the transfer of aggregates to the progeny cell either right before or during the loss event (Figure 3.9c). These data suggest that the partitioning error hypothesis for the mechanism of prion loss is consistent across SSB PrDs from different bacterial species.

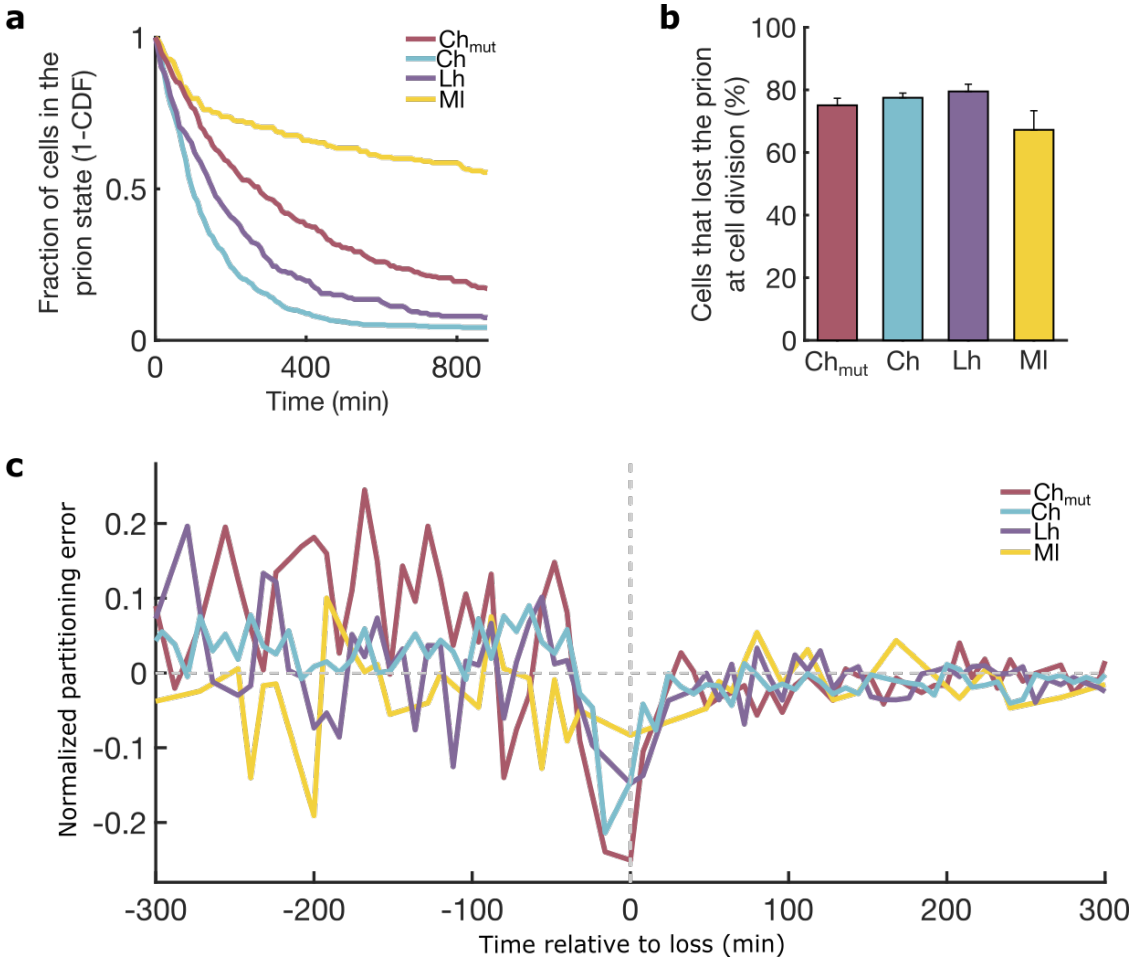

Figure 3.9: Prion loss kinetics of various SSB PrD orthologs. The loss distributions for SSB variants and the mutant show a large range in prion stability. The $t_{1/2}$ increased from 2.3 generations in *Ch*-SSB (blue line, n=1,014), 3.2 generations in *Lh*-SSB (purple line, n=352), 4.4 generations in Ch_{mut} (red line, n=438) and 17.9 generations in *Ml*-SSB (yellow line, n=135). b) Percentage of cells that lose the prion at cell division (Ch_{mut} n=247/329, *Ch*-SSB n=692/893, *Lh*-SSB n=229/288, *Ml*-SSB n=39/58). Error bars are the bootstrap estimates of the standard error of the mean. c) The median normalized partitioning error of cells that lost the prion state. The median was calculated for the following orthologs using cell traces that had more than 10 cell divisions occur at a single time point, *Ch*-SSB (blue line, n=893), Ch_{mut} (red line, n=329) and *Lh*-SSB (purple line, n=288). As the stability of the *Ml*-SSB prions result in very few loss events, the median was calculated using cell traces that had at least 4 cell divisions occur at a single time point (n=58 traces).

3.4.1 The SSB mutant can re-form prion aggregates after loss events

The mutant was found to form blue colonies on our indicator plates without ever interacting with the New1 initiation factor. We hypothesized that the Ch_{mut} SSB protein either aggregates at high concentration, or spontaneously folds into a prion conformation at a much higher rate than the native *Ch*-SSB. In the plate assays, colonies were either all in the aggregated state at high induction levels, or all in the non-aggregated state at lower induction levels (unpublished results from the Hochschild lab). However, in our microfluidic experiments we observed that the SSB mutant lost the prion state similarly to the other orthologs (Figure 3.9), indicating that cells can be either in the aggregated or non-aggregated state at the same concentration of protein. Additionally, during our previous experiment with the mutant, we observed, on rare occasions, aggregates re-appearing several generations after a loss event (Figure 3.10, iii). The reappearance of aggregates after a loss event was not observed in any of the SSB orthologs. These particular traces were excluded from the calculation of the loss rate in the previous section.

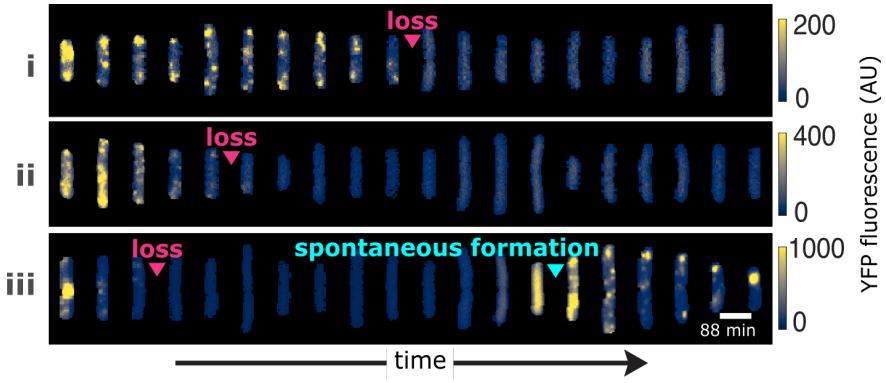

Figure 3.10: Spontaneous formation of prions in Ch_{mut}. Kymograph showing three different cell traces. In the first two traces (i and ii) the cells lose the prion (depicted by a pink triangle) and never regain it. The bottom trace (iii) shows spontaneous formation of aggregates (depicted by a blue triangle) several generations after a loss event. Images are shown 88 minutes apart.

Taken together, these results suggest that the Ch_{mut} can spontaneously adopt a prion conformation at a much higher rate than the SSB orthologs. Interestingly, human genetic prion diseases have been linked to a mutation in the PrP gene that causes a higher probability of spontaneous prion formation [128].

3.5 Support for distinct prion strains

To show the reproducibility of our experimental setup, the same colony was imaged and tracked in separate experiments on three different days. The prion loss distributions from these three separate experiments were almost identical, with half-lives for the prion state around 3 generations (Figure 3.11, colony A). There was no significant difference found between the prion loss distributions for these three different experiments (Kruskal-Wallis test, p=0.153). Using the same experimental setup, a different colony from the same plate as colony A displayed drastically different loss kinetics, with the prion aggregate half-life increasing four fold to ∼12 cell generations (Figure 3.11 colony B). The different loss kinetics for two *Lh*-SSB colonies provides further evidence for the existence of SSB prion variants. However, this would need to be investigated further.

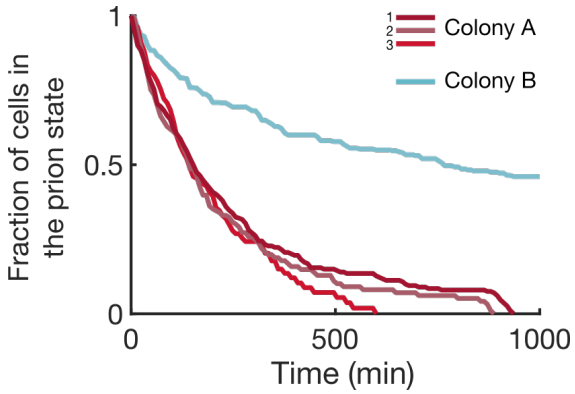

Figure 3.11: Different colonies display vastly different loss kinetics. a) Three different experiments (different days, different microlfuidic chips) with the same *Lh*-SSB colony produce almost identical loss curves (colony A, shades of red lines). The $t_{1/2}$ for colony A from experiments 1-3 is: 3.2 (n=352), 3.1(n=192), and 3.4 (n=309) cell generations respectively. A different colony selected from the same plate, colony B (blue line) displays stable prion propagation, with $t_{1/2}$ increasing to 11.9 generations (n=197).

3.6 Biological implications of the prion state

3.6.1 The impact of the prion state on doubling time

The yeast and bacterial prions identified thus far do not appear to cause major toxicity for the cells that harbour them. However, it is unclear if the presence of prions have an effect on the host's overall physiology. To determine if prions impose a burden on the cells that harbour them, we measured the doubling times (t_d) of cells with and without prions in our microfluidic device (Figure 3.12). Cells harbouring the small aggregate prions have a t_d ~3% (1.7 minutes) longer than cells without prions, while the cells with the old-pole aggregates grew with an additional ~2% (1.1 minutes) longer t_d than cells with the small aggregates (Figure 3.12). These results suggest that these prions confer a relatively small - but non negligible - penalty on the growth rate of their host.

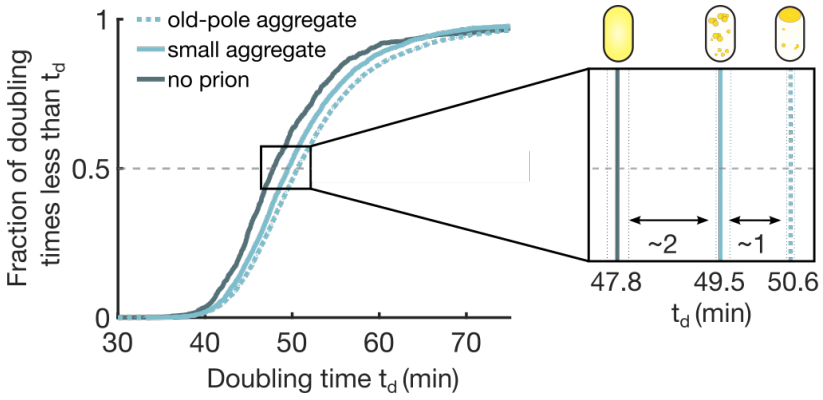

Figure 3.12: The *Ch*-SSB prion state confers a slight burden on cells that harbour them. The t_d of all cells were estimated by fitting an exponential growth rate for each division that occurred during the experiment. Empirical distribution function curves, with the median of the dataset represented by the grey dashed line on the y-axis (0.5). Cells with no prions have the fastest median t_d (47.8 min, n=6,767 time points, dark blue line), followed by cells harbour the small aggregate phenotype (t_d=49.5 min, n=19,880 time points, light blue line). The old-pole aggregate group has the longest median t_d at 50.6 minutes (n=61,696 time points, dotted light blue line). The inset shows a close up of when each group passes the median (grey dashed line), with the confidence interval lines running vertically around each curve in their respective colours.

3.6.2 Prion aggregates could provide protection to proteotoxic stress

Recently, cells containing non-specific protein aggregates were found to be more resistant to proteotoxic stress, such as exposure to hydrogen peroxide (H_2O_2), streptomycin, or heat shock, than cells without aggregates[129]. Govers et al. proposed this increase in resistance was due to the higher levels of specific protein quality control machinery (ClpB/P and DnaK/J) observed in cells containing protein aggregates[129]. Because our prion-containing cells display elevated ClpB expression, as observed using our transcriptional reporter plate assays, we hypothesized that bacterial prions could provide protection against proteotoxic stress.

To test this hypothesis, we treated prion-induced cells in our microfluidic device with a growth medium supplemented with a sublethal concentration of H_2O_2 (5 mM) for 20 minutes, before switching back to the standard growth medium. During H_2O_2 exposure, all cells stopped growing. This treatment was harsher than intended and resulted in very high cell death (Figure 3.13).

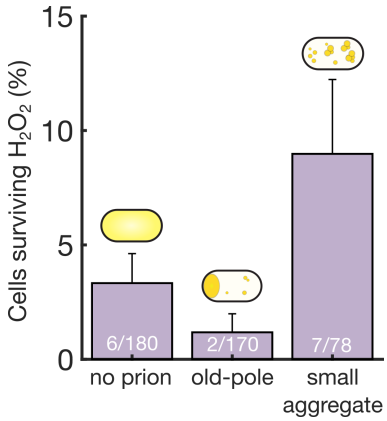

Figure 3.13: Prion cells show increased resistance to H_2O_2 exposure. Once half *Lh*-SSB cells had lost the prion state, they were exposed to 5mM of H_2O_2 for 20 minutes. Cells are considered prion-free if no aggregates were present in the cell for at least one division cycle before H_2O_2 exposure. Of the cells containing no prions, 3.3% survived treatment (n=6/180). 1.2% of cells containing the old-pole aggregates (n=2/170), and 9% of the small aggregate sub-population survived exposure to H_2O_2 (n=7/78), respectively. Numbers in white indicate the number of surviving cells out of the total cells in each group. Error bars are the bootstrap estimates of the standard error of the mean percentage of cells surviving H_2O_2 exposure.

Interestingly, the cells containing small prion aggregates were $\sim$2 times more likely to survive than cells without prions, whereas cells containing old-pole aggregates were $\sim$3 times less likely to survive. However, the results were not statistically significant, likely due to the small number of cells that survived. These preliminary results are nevertheless suggestive that prions could provide a protective role against proteotoxic stress. In the future, these experiments will be repeated with a sublethal stress that results in a $\sim$ 50% survival, which will greatly increase statistical power.

Chapter 4

Conclusion

In this thesis, we have presented the first characterization of prion propagation and loss at the single cell level. In order to do this, we built and implemented a rendition of a "mother machine" microfluidic device, enabling the tracking of hundreds of single bacterial cells in constant growth conditions. This microfluidic setup was then used to characterize and quantify prion loss in bacteria at the single cell level.

This thesis emphasizes the strength of our microfluidic platform for investigating the dynamics of prion inheritance in bacteria. Our first observations in the mother machine revealed two different SSB prion phenotypes: one with one large aggregate localized at the old-pole, and the other with several smaller aggregates dispersed throughout the cell. The old-pole sub-population displayed very stable prion propagation and an asymmetric division, creating one old-pole aggregate cell and one progeny cell harbouring prions with the small aggregate phenotype. This suggests that in a culture of growing cells, the old-pole phenotype would make up a smaller fraction of the population over time, yet could propagate the prion for long periods of time. These dynamics are obscured in the population-level stability experiments (e.g. plates). The importance of the old-pole aggregates in the survival of the prion phenotype in a growing population remains to be determined. We did not investigate if the old-pole aggregates can convert into the small aggregate phenotype, or vice-versa. We suspect that the old-pole aggregate is formed after an aggregate reaches a critical size, where it can no longer diffuse freely through the nucleoid and has limited chaperone accessibility. As there was not a complete separation between the two subpopulations using our classification (peak/average fluorescence ratio), we suggest further analysis methods to characterize the mobility of the prion state over time, thus enabling the investigation of the transition between

these states. In the future, alternative reporters of the prion state that do not depend on fluorescent protein fusion with the prion domain, such as transcriptional reporter, would strengthen the biological relevance of the old-pole aggregate.

Quantifying the loss kinetics of the small aggregate sub-population for all the SSB PrD orthologues (*Ch*-SSB, *Ml*-SSB, *Lh*-SSB) and Ch_{mut} showed that the small aggregate prion state is lost following an exponential decay (i.e. a memoryless process). Investigating the mechanisms of prion loss revealed that partitioning errors caused asymmetric segregation of the prion aggregates into the progeny cell at or before the time of prion loss. The *Ch*-SSB progeny cells that received prion aggregates after a loss event in the mother cell continued to propagate the prion state for the time we could track them. Additionally, the majority of loss events occurred at cell division in all of the SSB PrD orthologues and the mutant. Therefore, we conclude that prion loss is caused by partitioning errors for the prion domains studied. This is consistent with what was observed in yeast, where prion variants with smaller but more numerous aggregates, which would be predicted to have smaller partitioning errors, were more stable than prions with larger aggregates[27]. In the future, we suggest characterizing the distribution of aggregate size using partitioning errors or image analysis methods such as Spatial Intensity Distribution Analysis (SpIDA)[130] and correlating it with the stability, to further confirm the role of partitioning error in the stability of the prion. Because bacteria are smaller and divide more rapidly the yeast, we would generally expect bacterial prions to be more affected by partitioning errors, as these errors scale with the inverse of the square root of the number of molecules[?] . This could tentatively explain why the bacterial prions observed so far appear to be less stable than the yeast prions.

Our preliminary results that different cell colonies harbouring the *Lh*-SSB prions displayed drastically different loss kinetics provided support for the existence of bacterial prion variants. This suggests that the *Lh*-SSB protein can convert into structurally distinct prion variants with varying stabilities, a phenomenon well documented in mammalian and yeast prions[16,20–22]. The different prion stabilities observed within and across the SSB orthologues likely result from different rates of elongation and fragmentation in the prion propagation cycle, as observed with the yeast $[PSI^+]$ prion variants[27]. To further investigate the existence of SSB prion variants, we suggest the following experiment. First, the variants should be "purified", as multiple prion variants can co-exist temporarily in the cells upon prion induction before one variant out-competes the others[84,131]. To accomplish this, we suggest re-plating several prion-positive colonies. The prion loss kinetics of the second round of prion-positive colonies, which we call R2 colonies, could then be quantified using our

microfluidic platform. We hypothesize that different R2 colonies will display different loss kinetics. The same colonies used in the microfluidic device will be passaged several more times (e.g. to create R5 colonies), which will again have their loss kinetics measured. We expect identical loss kinetics of each colony to its parent colony in the first experiment. This would show that the different loss kinetics are self-propagating, thus confirming the existence of SSB prion variants. We could then characterize the loss kinetics for each variant identified in each orthologue, to see if, despite their very different amino acid sequence, the properties of their prion domains are similar.

As expected, we observed that Ch_{mut} could spontaneously form aggregates after a loss event, a phenomenon not observed in any of the SSB orthologs. We hypothesize that this genetic mutant is similar to the genetic prion diseases, where a mutation increases the probability of the spontaneous formation of a specific prion variant [128]. We thus hypothesize that the SSB mutant also adopts one specific strain. To provide further evidence for the prion properties of the mutant and the existence of prion variants, we suggest analysing the loss kinetics for several different colonies. If the properties of Ch_{mut} are similar to that of genetic prion diseases, i.e. it spontaneously adopts one specific prion aggregate structure, we expect different Ch_{mut} colonies to always display the same loss kinetics.

We observed that the *Ch*-SSB small aggregate prions impose a small yet meaningful cost on the growth rate of their host, with a slightly larger burden imposed for cells harbouring the old-pole aggregates. With the biological function of many prions currently unknown, we investigated if the slight burden imposed on cell growth could be a trade-off for a selective advantage in the population. To that end, we attempted to recreate the fitness experiments conducted by Govers et al. on the role protein aggregates play in resistance to proteotoxic stressors [129]. Our preliminary results suggested that cells harbouring the small aggregate prions were $\sim$2 times more likely to survive H_2O_2 exposure than prion-free cells, indicating the SSB prion may provide a protective role against proteotoxic stress. Although our sample size was too small, our observations provide motivation to continue to investigate the resistance prion-containing cells may have to H_2O_2 and other proteotoxic stressors such as heat shock and streptomycin exposure. In future experiments, we suggest measuring the time to recovery from the stress (H_2O_2 or streptomycin) along with the survival rate, and using stress that results in $\sim$ 50 % survival rate to increase the sample size.

With increasing evidence that prion inheritance is a conserved cellular process across all domains of life [52], future studies using our microfluidic platform will continue to shed light on the mechanisms of prion propagation for both functional and pathogenic

prions.

Chapter 5

Materials and methods

5.1 Microfluidics

5.1.1 Photolithography

The finalized template designed by Giselle McCallum was sent to Toppan Photomasks Inc. to create the quartz photomask required for standard photolithography. The wafers used throughout this thesis were fabricated at the McGill Nanotools microfabrication facility (Montréal, Canada), a class 100 cleanroom, to reduce particulate contamination while maintaining constant humidity, pressure and temperature. The following recipe was used to create the 1.0µm tall template:

Layer 1: Cell trenches

The 4 inch silicon wafer was washed with acetone, isopropyl alochol (IPA) and deionized water, then dehydrated at 150°C for 15 minutes. The wafer was then cleaned with oxygen plasma in the DSB6000 Oxygen Asher. 5mL of photoresist (SU-8 2001, Microchem) was poured on the wafer and spun at two speeds (rotations per minute/acceleration/time): first at 500/87/10 then 1500/348/60 (Laurell Spin Coater). The wafer is then soft baked (SB) for: 1 minute at 65°C, 3 minutes at 95°C, 1 minute at 65°C before exposed to UV light (42.5 mW/cm^2) for 1.5 seconds using the EVG620 photomask aligner. UV exposure was followed by a post exposure bake (PEB) of 1 minute at 65°C, 20 minutes at 95°C, 1 minute at 65°C. Excess SU-8 was washed away by swirling gently in dish filled with SU-8 developer

for 30 seconds, then rinsed immediately with more developer followed by IPA for 10 seconds. A final hard bake (HB) for 1 minute at 65°C, 10 minutes at 150°C, 1 minute at 65°C sets the first layer, allowing the height to be measured using the Ambios XP200 profiler.

Layer 2: Feeding channel

A second coating of photoresist (5mL SU-8 2015, Microchem) was applied at two speeds (rotations per minute/acceleration/time): first at 500/87/10 then 3000/348/60 (Laurell spin coater). SB for: 1 minute at 65°C, 4 minutes at 95°C, 1 minute at 65°C. A developer soaked swab was used to clean off the photoresist from the alignment markers, followed by a second SB for the same amount of time. The second photomask was aligned with the features on the wafer and exposed to UV light (42.5 mW/cm^2) for 3.4 seconds (EVG620 photomask aligner). PEB for 1 minute at 65°C, 4 minutes at 95°C, 1 minute at 65°C. Washed away excess photoresist by swirling gently in dish filled with SU-8 developer for 1 minute and 30 seconds, then rinsed immediately with more developer followed by IPA for 10 seconds. A final HB for 1 minute at 65°C, 15 minutes at 150°C, 1 minute at 65°C completes the wafer/mold manufacturing.

5.1.2 Soft lithography

Soft lithography is the microfabrication technique of casting an elastomer onto a completed wafer to imprint the microstructure design into it. As the master mold wafers are designed to be reused, before the initial PDMS casting the wafer surface is modified by a chlorosilane treatment (trichloro-1,1,2,2-perfluorooctyl-silane) forming a monoloayer with super hydrophobic properties[120]. This ensures consistent easy release of PDMS slabs from the wafer. The PDMS slab (Sylgard 184 Silicon Elastomer) was mixed at a 10:1 (monomer:curing agent) ratio, poured on top of the 1.0 µm tall master mold and degassed for one hour at room temperature before baking for an additional 1.5 hours at 65°C. After careful remover of the PDMS slab from the master mold/wafer, an individual device (PDMS chip) is cut out with a razer blade. The inlet and outlet holes (for the media to flow though) were punched with a 0.75 mm biopsy puncher (World Precision Instruments).

5.1.3 Microfluidic device construction

The PDMS chip was sonicated in isopropyl alcohol for 30 minutes and dried in a 65°C oven. The final step of manufacturing an individual microfluidic device is to create a strong, watertight seal between the PDMS and a glass interface[120,132]. Glass coverslips (Fischer Scientific: 22x40 mm #1.5) are cleaned with potassium hydroxide, ensuring clear microscopy images can be taken. To maintain biocompatibility between the glass and PDMS structures the plasma treatment protocol from the Singh Center for Nanotechnology[133] was followed: Oxygen flow rate at 45 sccm, power at 30W for 15 seconds (Tergeo Plasma Cleaner, PIE Scientific). The completed microfluidic device is heated to reinforce the plasma bonding at 100°C for 10 minutes, then 65°C for 30 minutes.

5.2 Experimental setup

5.2.1 Strain construction

With the goal of using these strains in the mother machine microfluidic device, the motility gene *motA* was deleted from our background K-12 MG1655 *E. coli* strain to ensure the bacteria cannot swim out of the cell trenches[134]. The $P_{clpB} - lacZ$ reporter used for the prion detection assay was assembled on the F' episome[65]. Additionally our background stain contains the P_{rpsL}-mSCFP3A fusion integrated at the Tn7 site to constitutively produce CFP, which was used to segment the cells during analysis.

Table 5.1: List of strains used in Chapter 3

Strain	Parent	Genotype	Plasmids
LPT37	MG1655	P_{rpsL}-mSCFP3, △motA	
BLS80	LPT37	$P_{clpB} - lacZ$ on F',△lacYZA	pNew1, pSSB
KLJ15	BLS80	$P_{clpB} - lacZ$ on F',△lacYZA	pCh_{mut}-SSB

The BLS80 strain and the plasmids used in this thesis were constructed by Dr. Benjamin Lennart Springstein (Table 5.1). The New1-mScarlet fusion containing plasmid has a temperature sensitive origin of replication (pSC101-ts) and the isopropyl β-d-1-thiogalactopyranoside (IPTG) inducible promoter, tac (P_{tac}). All of the

SSB-YFP(mEYFP) orthologues were constructed on the BR plasmid, and also have the IPTG inducible tac promoter.

Table 5.2: List of plasmids used in Chapter 3.

Plasmid	Ori	Antibiotic resistance	Genotype
pNew1	pSC101-ts	Cam	P_{tac}-New1-mScarlet-1
p*Ch*-SSB	pBR	Carb	P_{tac}-His6x-eYFP-*Ch*-SSB-PrD
pCh_{mut}-SSB	pBR	Carb	P_{tac}-His6x-eYFP-*Ch*-SSB-PrD-mutant
p*Lh*-SSB	pBR	Carb	P_{tac}-His6x-eYFP-*Lh*-SSB-PrD
p*Ml*-SSB	pBR	Carb	P_{tac}-His6x-eYFP-*Ml*-SSB-PrD

5.2.2 Cell preparation and culturing

The backgrount strain BLS80 used in Chapter 3 was made chemically competent following the transformation storage solution (TSS) method. Prior to every microfluidic experiment, the appropriate SSB and New1 plasmids were co-transformed into the TSS competent cells (heatshock at 42°C for 30 seconds, incubate on ice for 2 minutes) with an extended recovery time of two hours at 30°C before plating on LB agar plates containing the appropriate antibiotics. After overnight growth at 30°C, a colony selected from the transformation plate was grown in liquid LB containing antibiotics and 10µM IPTG to induce the prion state, again at 30°C. After 16 hours of growth, the cells are plated on LB agar containing 10µM IPTG, X-gal (40µg/mL), Phenylethyl-β-D-thiogalactopyranoside (TPEG) (500µM), and the antibiotics kanamycin and carbenicillin. As all cells express ClpB to some extent, TPEG is included in the plates as a competitive inhibitor of the enzyme β-galactosidase, making it easier to distinguish the prion containing (blue, which express ClpB at a higher level) from the prion-free (pale) colonies. Without the addition of TPEG, after 24 hours of growth at 37°C (to lose the New1 plasmid) all of the colonies are a shade of blue. Typically around 15 prion containing colonies (blue) were cultured for 16 hours in imaging medium (M9 salts, 0.2% (w/v) glucose, 1 mM MgSO4, 0.1 mM CaCl2, 20µg/mL uracil, 0.2 g/L casamino acids and 0.85 g/L Pluronic F-108 (Sigma Aldrich)) at 30°C. Each culture was checked using fluorescent microscopy to confirm SSB prion presence and the absence of New1. After prion content was confirmed, cells were loaded into the main feeding channel of a microlfuidic chip and then centrifuged into the cell trenches (5000g for 10 minutes). A syringe pump (New Era Pump System) was connected to the inlet hole via

flexible plastic tubing (Tygon) to provide the cells with fresh imaging medium, pumped at 5 µl/min for the duration of an experiment (Figure 5.1).

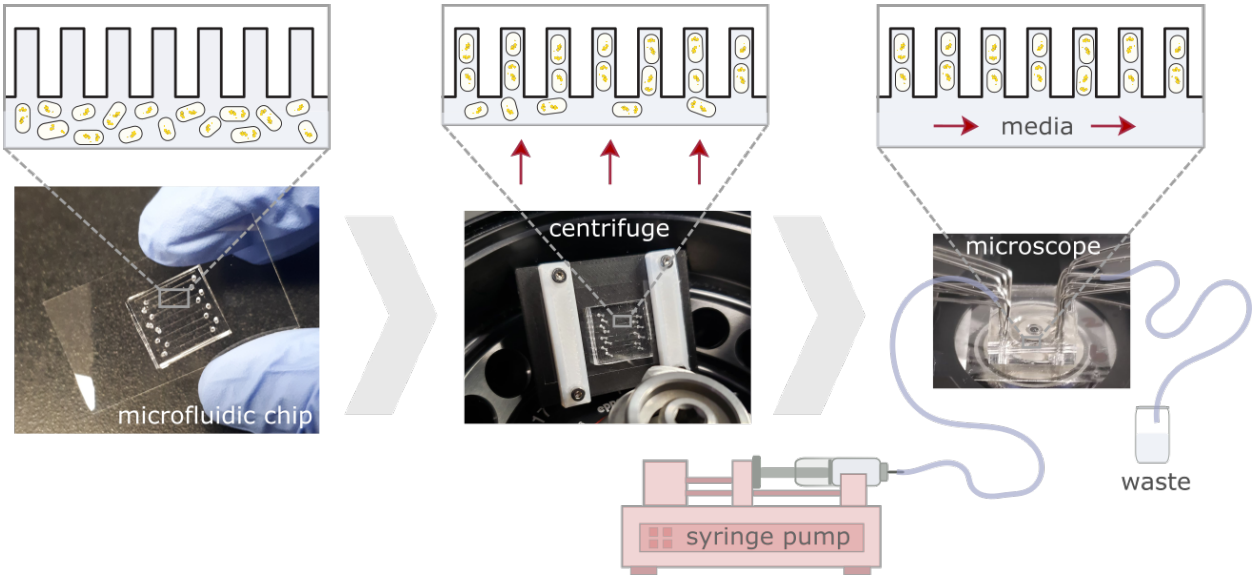

Figure 5.1: Microfluidic chip loading overview. Cells are loaded into the main feeding channel and then pushed into the cell trenches via centrifugal force. A syringe pump is setup to pump fresh media though the feeding channel for the duration of an experiment.

5.2.3 Imaging protocol

All microscopy was conducted using a Zeiss Axio Observer inverted microscope equipped with a 63x Plan-Apochromat M27 oil objective (NA 1.40), an Orca Flash 4.0 LT camera (Hamamatsu), and an LED epifluorescence illuminator (Collibri 7), inside a temperature controlled incubation chamber set at 30°C. Exposure time (100ms) and light intensity (10-20%) were low to reduce photobleaching, with 16-bit CZI (later converted to TIFF) images taken every 8 minutes using the Colibri 7 (Zeiss) 91 HE filter set. Focal drift was corrected automatically with the Definite Focus 2 (Zeiss) monitoring and compensation system using an infrared laser (850 nm).

5.3 Data analysis

5.3.1 Image segmentation and tracking analysis pipeline

All analysis was completed using MATLAB (Mathworks) with the segmentation and tracking scripts provided by Dr. Laurent Potvin-Trottier. Once imaging finished, cell segmentation and lineage tracing was completed using a previously described Matlab analysis pipeline[135] in which a pixel mask is created to define the boundaries of each cell based on the constitutively expressed CFP. Within the pixel mask, data (cell size, fluorescence, etc.) was extracted and the mother cells from consecutive frames were stitched together to create a continuous time trace for each individual cell (Figure 5.2).

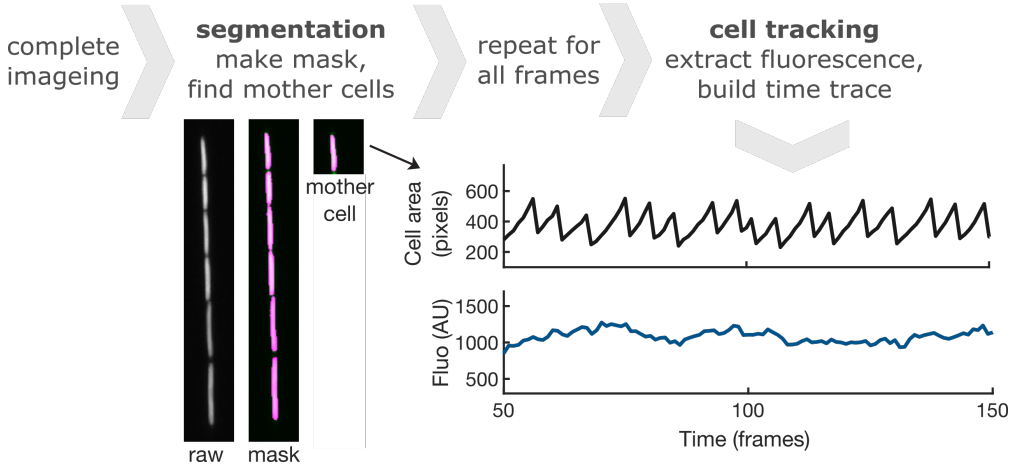

Figure 5.2: Image analysis pipeline overview. An example of a single trench with the raw fluorescence image (grey) and the pixel mask (pink), with the mother cell pixel mask overlaid on top of the raw image (pink on green). Example time trace of cell size and average fluorescence of a single cell over time.

We define the following values for the segmented data:

- **Average fluorescence**: The mean pixel value (YFP or CFP) within the cells segmentation pixel mask.
- **Peak fluorescence**: The median value of the brightest 10% of pixels within the segmentation pixel mask.
- **Cell division**: A division event occurs if the area of a cell dropped to less than 60 % of its previous value.

5.3.2 Prion spot finding and phenotype identification

Spots were identified within cells by finding peaks of YFP fluorescence using the local maxima, which produced an (x,y) value for the center of a spot along with the number of spots present in a cell. We use the peak finding open source function 'findpeaks' (Nathaniel C. Yoder), that uses a low pass Gaussian filter (5x5 pixel size, standard deviation of 0.95) to emphasize point spread function-size features.

A prion loss event is defined as the first frame in a run of at least 8 consecutive images without any spots. If the function finds a spot after 8 consecutive zero spot frames, the entire trace is excluded from the analysis. These traces were typically found to contain segmentation errors and pixels from other cells. Example kymographs in Figure 5.3 shows the raw images of cells leading up to and after a loss event.

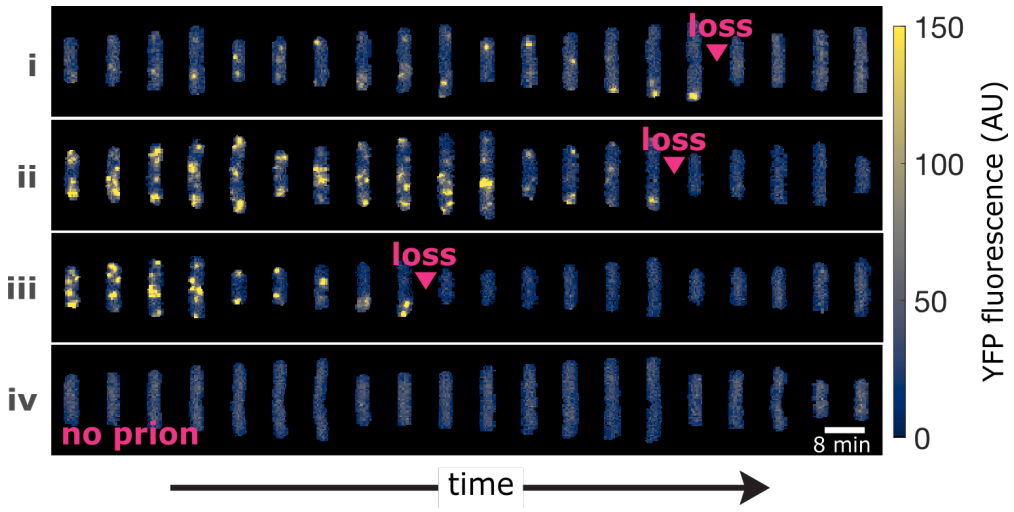

Figure 5.3: A spot finding algorithm correctly identifies cells in the prion state. The first three kymographs show prion loss events as identified by our analysis, symbolized with a pink triangle. The bottom trace shows a cell that never had prions. Images were taken 8 minutes apart.

5.3.3 Determining the start time for the analysis

Analysis of our raw data revealed a delay at the beginning of the experiment before cells start to lose the prion state (Figure 5.3a). Indeed, cells need time to adjust to growing in the microfluidic device, resulting in many 'mother machine' microfluidic experimental

procedures waiting several hours (e.g. 2-14) before starting imaging after the cells are loaded[98,136–139]. As we did not want to risk missing prion loss events, imaging started almost immediately after loading in all of our microfluidic experiments. Additionally, as stationary phase culture was used, there is a lag time in cell growth and transcriptional activity as cells exit stationary phase in the device[98,140], which may contribute to the delay of prion loss events at the beginning of an experiment. We observed that the concentration of the prion domain (YFP) was much higher at the beginning of the experiments, likely due to cells exiting stationary phase, and its levels stabilized after a few generations. To accommodate for these transitions, the first few generations of data collected during an experiment were excluded from the prion loss kinetics analysis. The analysis start time was determined from the mean residual lifetime trace of the prion state, as previously described[135], where the mean residual lifetime R at time t determines the expected time left $(T - t)$ in the prion state given a cell has propagated them for a time period t :

$$R(t) = E[T - t|T > t]$$

Memoryless processes produce a horizontal flat residual lifetime, whereas a deterministic timer-like behaviour produces a linearly decreasing curve with a slope of -1, as seen at the beginning of the experiment when cells are coming out of stationary phase (Figure 5.4b)[135].

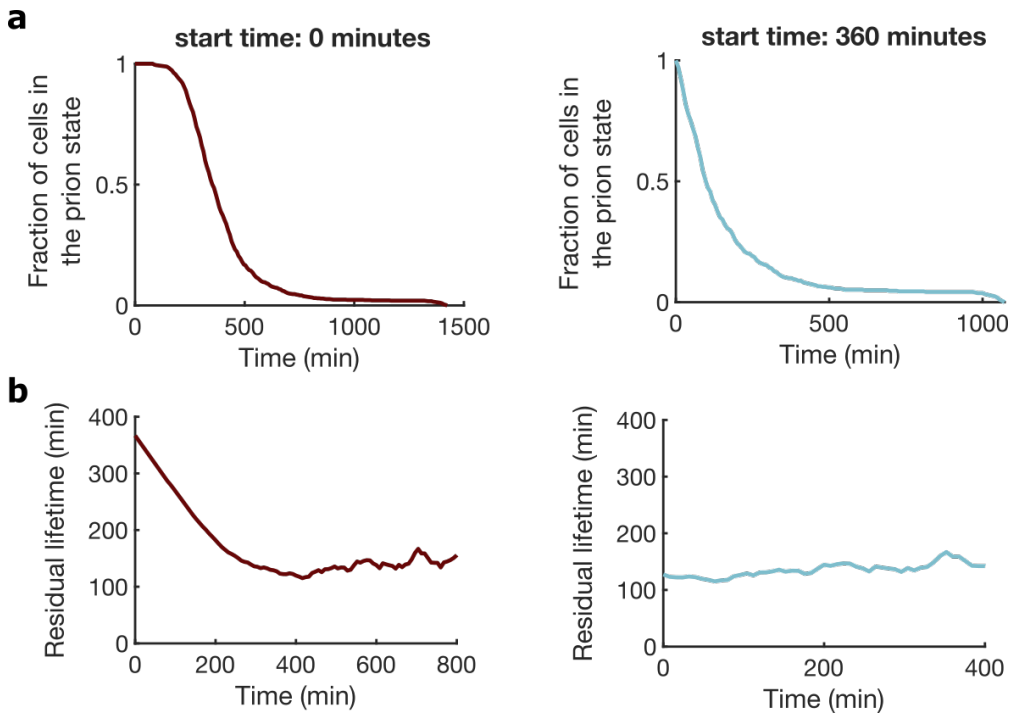

Figure 5.4: Delaying analysis start times based on the residual lifetime estimate. a) Fraction of cells in the prion state at the time of imaging (left), and at 360 minutes after imaging began (right). The plot starting at 360 minutes is the same plot as in Figure 3.6a. b) The residual lifetime at the above start times. Plots with a start time of 0 minutes are red, and plots with a start time of 360 minutes are blue.

Every experiment's start time was slightly different as imaging would begin at varying times after loading cells into the device and cells were grown for slightly different time periods overnight. Therefore, the start time for each microfluidic experiment was determined following the process described above (Table 5.3).

Table 5.3: List of the analysis start times for different experiments and the associated figures.

Strain	Experiment	Start time (image number)	Figures
Ch-SSB	MM27	45	3.3-3.9, 3.12
Ch_{mut}-SSB	MM28	36	3.9
Lh-SSB	MM29	32	3.11
Lh-SSB	MM30	40	3.11
Lh-SSB, *Ml*-SSB	MM31	42	3.9, 3.11
Lh-SSB	MM33	29	3.11

Chapter 6

Appendix: Supplementary figures

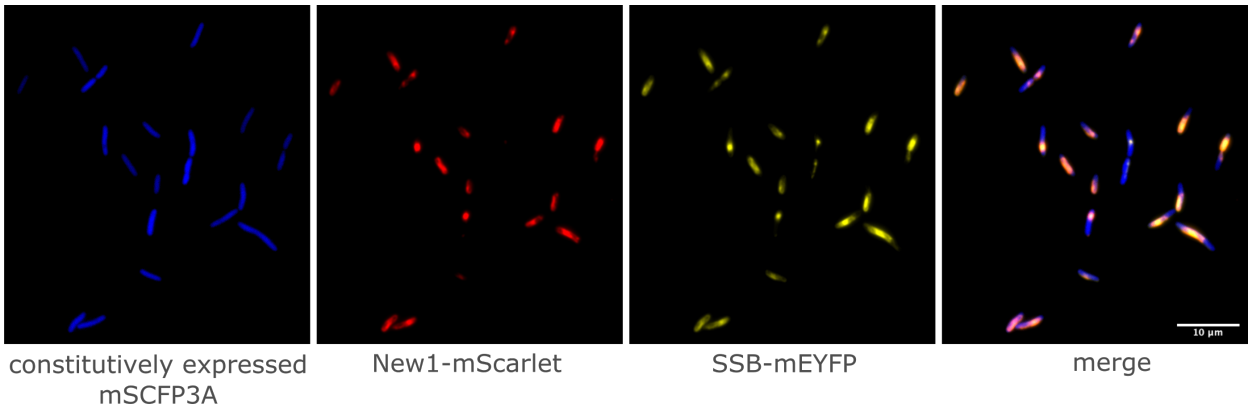

Figure 6.1: Prion visualization via fluorescence microscopy. Fluorescent image of *E. coli* cells containing both New1 and SSB plasmids

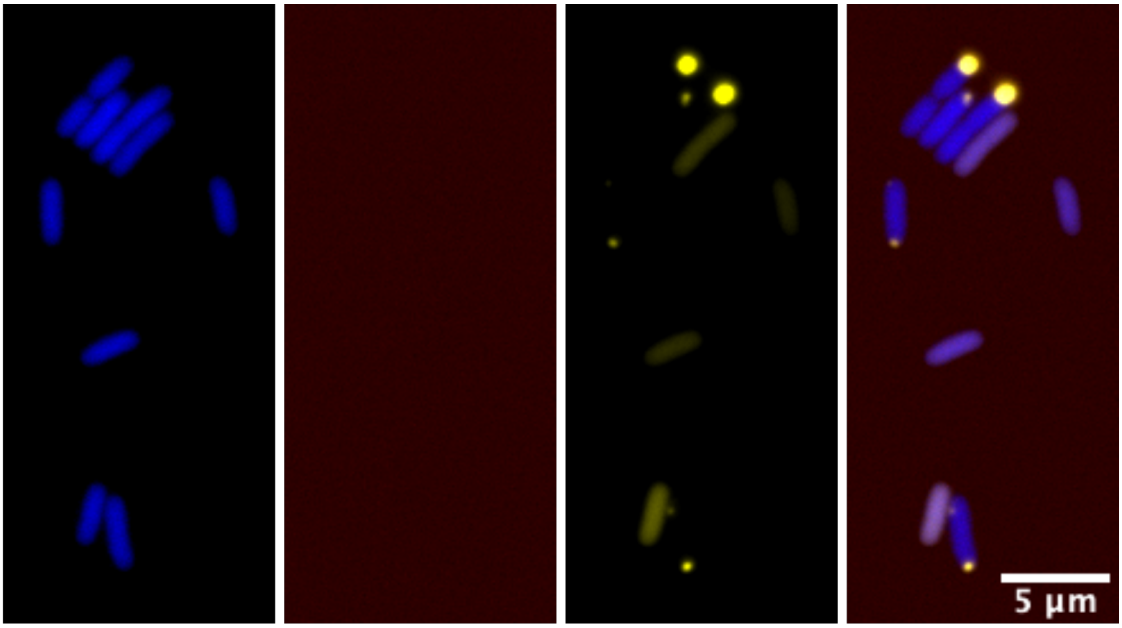

Figure 6.2: Microscopy confirmation of New1 loss. Fluorescent image of *E. coli* cells cured of New1 with no red fluorescence detectable. Cells continue to produce SSB aggregates (yellow foci).

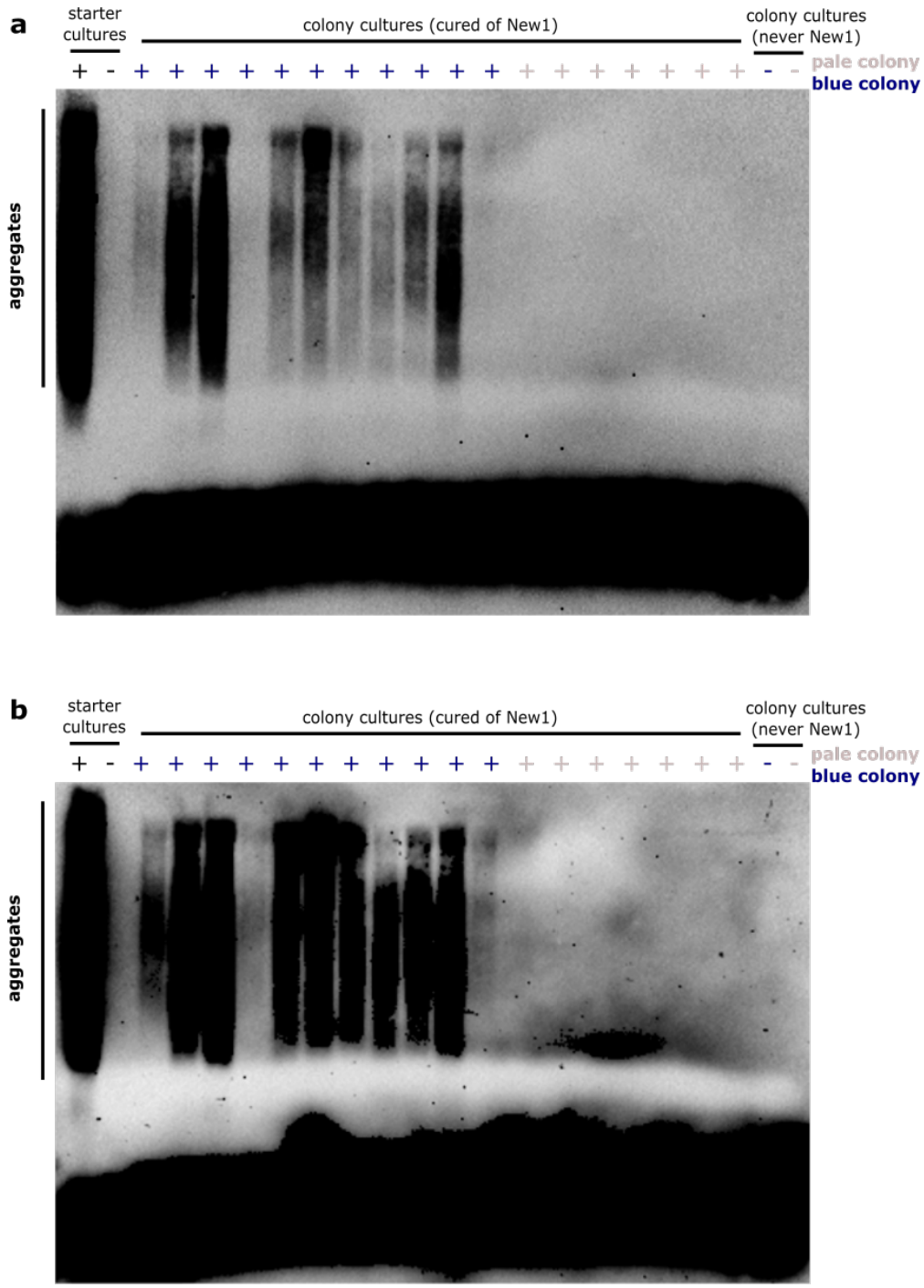

Figure 6.3: Western blot confirms presence of prion aggregates in blue colonies. a) Blue colonies contain SDS-insoluble *Ch*-SSB aggregates whereas pale colonies contain only soluble *Ch*-SSB proteins. b) An extended exposure reveals that all of the blue colonies have at least a pale SDS-stable smear. The SDD-AGE from cell lysates was prepared by Dr. Benjamin Lennart-Springstein according to Fleming et al. (2019) with SDS-stable smears detected using anti-His antibody[65].

Bibliography

[1] T. H. Morgan. The Theory of the Gene. *Am. Nat.*, 51(609):513–544, sep 1917. doi: 10.1086/279629.

[2] Oswald T. Avery, Colin M. Macleod, and Maclyn McCarty. Studies on the chemical nature of the substance inducing transformation of pneumococcal types: Induction of transformation by a desoxyribonucleic acid fraction isolated from pneumococcus type iii. *J. Exp. Med.*, 79(2):137–158, feb 1944. doi: 10.1084/jem.79.2.137.

[3] A. D. Hershey and M. Chase. Independent functions of viral protein and nucleic acid in growth of bacteriophage. *J. Gen. Physiol.*, 36(1):39–56, sep 1952. doi: 10.1085/jgp.36.1.39.

[4] Francis Crick. On protein synthesis. *Symp Soc Exp Biol*, 1958.

[5] Francis Crick. Central Dogma of Molecular Biology. *Nat. 1970 2275258*, 227(5258): 561–563, 1970. doi: 10.1038/227561a0.

[6] Paul Brown and Raymond Bradley. 1755 and all that: A historical primer of transmissible spongiform encephalopathy, dec 1998.

[7] Hans Gerhard Creutzleldt. Uber eine eigenartige herdfSrmige Erkrankung des Zentral-nervensystems. (Vorl˜ufige Mitteilung.) 1). *Z Gesamte Neurol Psy.*, (57):1–18, 1920.

[8] A Jakob. Uber eigenartige Erkrankungen des Zentralnervensystems mit bemerkenswertem anatomischen Befunde. *Gesamte Neurol Psy*, (64):147–228, 1921.

[9] D. C. Gajdusek and V. Zigas. Degenerative Disease of the Central Nervous System in New Guinea. *N. Engl. J. Med.*, 257(20):974–978, nov 1957. doi: 10.1056/nejm195711142572005.

[10] Mark D. Zabel and Crystal Reid. A brief history of prions, dec 2015.

[11] Kurt Schneider, Heiner Fangerau, Britta Michaelsen, and Wolfgang H.M. Raab. The early history of the transmissible spongiform encephalopathies exemplified by scrapie. *Brain Res. Bull.*, 77(6):343–355, dec 2008. doi: 10.1016/j.brainresbull.2008.09.012.

[12] Tikvah Alper, D. A. Haig, and M. C. Clarke. The exceptionally small size of the scrapie agent. *Biochem. Biophys. Res. Commun.*, 22(3):278–284, feb 1966. doi: 10.1016/0006-291X(66)90478-5.

[13] Stanley B. Prusiner. Novel proteinaceous infectious particles cause scrapie. *Science (80-.).*, 216(4542):136–144, 1982. doi: 10.1126/science.6801762.

[14] David M. Garcia and Daniel F. Jarosz. Rebels with a cause: Molecular features and physiological consequences of yeast prions. *FEMS Yeast Res.*, 14(1):136–147, feb 2014. doi: 10.1111/1567-1364.12116.

[15] Simon Alberti, Randal Halfmann, Oliver King, Atul Kapila, and Susan Lindquist. A Systematic Survey Identifies Prions and Illuminates Sequence Features of Prionogenic Proteins. *Cell*, 137(1):146–158, apr 2009. doi: 10.1016/j.cell.2009.02.044.

[16] Tessier PM and Lindquist S. Unraveling infectious structures, strain variants and species barriers for the yeast prion [PSI+]. *Nat. Struct. Mol. Biol.*, 16(6):598–605, jun 2009. doi: 10.1038/NSMB.1617.

[17] Walker S. Jackson, Andrew W. Borkowski, Henryk Faas, Andrew D. Steele, Oliver D. King, Nicki Watson, Alan Jasanoff, and Susan Lindquist. Spontaneous generation of prion infectivity in fatal familial insomnia knock-in mice. *Neuron*, 63(4):438, aug 2009. doi: 10.1016/J.NEURON.2009.07.026.

[18] Zhihong Zhang, Yi Zhang, Fei Wang, Xinhe Wang, Yuanyuan Xu, Huaiyi Yang, Guohua Yu, Chonggang Yuan, and Jiyan Ma. De novo generation of infectious prions with bacterially expressed recombinant prion protein. *FASEB J.*, 27(12):4768–4775, dec 2013. doi: 10.1096/fj.13-233965.

[19] Marcelo A. Barria, Abhisek Mukherjee, Dennisse Gonzalez-Romero, Rodrigo Morales, and Claudio Soto. De Novo Generation of Infectious Prions In Vitro Produces a New Disease Phenotype. *PLOS Pathog.*, 5(5):e1000421, may 2009. doi: 10.1371/JOURNAL.PPAT.1000421.

[20] S. B. Prusiner. Scrapie prions, 1989.

[21] Natallia Makarava and Ilia V. Baskakov. The Same Primary Structure of the Prion Protein Yields Two Distinct Self-propagating States *. *J. Biol. Chem.*, 283(23): 15988–15996, jun 2008. doi: 10.1074/JBC.M800562200.

[22] Jed J W Wiltzius, Meytal Landau, Rebecca Nelson, Michael R Sawaya, Marcin I Apostol, Lukasz Goldschmidt, Angela B Soriaga, Duilio Cascio, Kanagalaghatta Rajashankar, and David Eisenberg. Molecular mechanisms for protein-encoded inheritance. *Nat. Struct. Mol. Biol. 2009 169*, 16(9):973–978, aug 2009. doi: 10.1038/nsmb.1643.

[23] Jiri Safar, Peter P. Roller, D. Carleton Gajdusek, and Clarence J. Gibbs. Thermal stability and conformational transitions of scrapie amyloid (prion) protein correlate with infectivity. *Protein Sci.*, 2(12):2206–2216, 1993. doi: 10.1002/PRO.5560021220.

[24] Richard A. Bessen, David A. Kocisko, Gregory J. Raymond, Santosh Nandan, Peter T. Lansbury, and Byron Caughey. Non-genetic propagation of strain-specific properties of scrapie prion protein. *Nature*, 375(6533):698–700, 1995. doi: 10.1038/375698a0.

[25] Jiri Safar, Holger Wille, Vincenza Itri, Darlene Groth, Hana Serban, Marilyn Torchia, Fred E. Cohen, and Stanley B. Prusiner. Eight prion strains have PrPSc molecules with different conformations. *Nat. Med. 1998 410*, 4(10):1157–1165, oct 1998. doi: 10.1038/2654.

[26] Glenn C. Telling, Piero Parchi, Stephen J. DeArmond, Pietro Cortelli, Pasquale Montagna, Ruth Gabizon, James Mastrianni, Elio Lugaresi, Pierluigi Gambetti, and Stanley B. Prusiner. Evidence for the conformation of the pathologic isoform of the prion protein enciphering and propagating prion diversity. *Science*, 274(5295): 2079–2082, dec 1996. doi: 10.1126/SCIENCE.274.5295.2079.

[27] Motomasa Tanaka, Sean R. Collins, Brandon H. Toyama, and Jonathan S. Weissman. The physical basis of how prion conformations determine strain phenotypes. *Nat. 2006 4427102*, 442(7102):585–589, jun 2006. doi: 10.1038/nature04922.

[28] Fabrizio Chiti and Christopher M. Dobson. Protein misfolding, functional amyloid, and human disease, jun 2006.

[29] Tuomas P. J. Knowles, Michele Vendruscolo, and Christopher M. Dobson. The amyloid state and its association with protein misfolding diseases. *Nat. Rev. Mol. Cell Biol. 2014 156*, 15(6):384–396, may 2014. doi: 10.1038/nrm3810.

[30] Jean D. Sipe, Merrill D. Benson, Joel N. Buxbaum, Shu-ichi Ikeda, Giampaolo Merlini, Maria J. M. Saraiva, and Per Westermark. Amyloid fibril proteins and amyloidosis: chemical identification and clinical classification International Society of Amyloidosis 2016 Nomenclature Guidelines. *https://doi.org/10.1080/13506129.2016.1257986*, 23 (4):209–213, oct 2016. doi: 10.1080/13506129.2016.1257986.

[31] Tricia R Serio. [PIN+]ing down the mechanism of prion appearance. *FEMS Yeast Res.*, 18(3):26, may 2018. doi: 10.1093/FEMSYR/FOY026.

[32] T. R. Serio, A. G. Cashikar, A. S. Kowal, G. J. Sawicki, J. J. Moslehi, L. Serpell, M. F. Arnsdorf, and S. L. Lindquist. Nucleated conformational conversion and the replication of conformational information by a prion determinant. *Science (80-.).*, 289(5483):1317–1321, aug 2000. doi: 10.1126/SCIENCE.289.5483.1317.

[33] Margaret Sunde, Louise C. Serpell, Mark Bartlam, Paul E. Fraser, Mark B. Pepys, and Colin C.F. Blake. Common core structure of amyloid fibrils by synchrotron X-ray diffraction. *J. Mol. Biol.*, 273(3):729–739, oct 1997. doi: 10.1006/JMBI.1997.1348.

[34] Tuomas P. Knowles, Anthony W. Fitzpatrick, Sarah Meehan, Helen R. Mott, Michele Vendruscolo, Christopher M. Dobson, and Mark E. Welland. Role of intermolecular forces in defining material properties of protein nanofibrils. *Science (80-.).*, 318(5858): 1900–1903, dec 2007. doi: 10.1126/SCIENCE.1150057.

[35] Raimon Sabate, Frederic Rousseau, Joost Schymkowitz, Cristina Batlle, and Salvador Ventura. Amyloids or prions? That is the question. *Prion*, 9(3):200, jan 2015.

[36] Anupam K. Chakravarty, Tina Smejkal, Alan K. Itakura, David M. Garcia, and Daniel F. Jarosz. A non-amyloid prion particle that activates a heritable gene expression program. *Mol. Cell*, 77(2):251, jan 2020. doi: 10.1016/J.MOLCEL.2019.10.028.

[37] Janice Villali, Jason Dark, Teal M. Brechtel, Fen Pei, Suzanne S. Sindi, and Tricia R. Serio. Nucleation seed size determines amyloid clearance and establishes a barrier to prion appearance in yeast. *Nat. Struct. Mol. Biol.*, 27(6):540–549, jun 2020. doi: 10.1038/s41594-020-0416-6.

[38] Joanna Masel, Vincent A.A. Jansen, and Martin A. Nowak. Quantifying the kinetic parameters of prion replication. *Biophys. Chem.*, 77(2-3):139–152, mar 1999. doi: 10.1016/S0301-4622(99)00016-2.

[39] Meredith L. Greer, Laurent Pujo-Menjouet, and Glenn F. Webb. A mathematical analysis of the dynamics of prion proliferation. *J. Theor. Biol.*, 242(3):598–606, oct 2006. doi: 10.1016/J.JTBI.2006.04.010.

[40] Zachary H. Harvey, Yiwen Chen, and Daniel F. Jarosz. Protein-Based Inheritance: Epigenetics beyond the Chromosome, jan 2018.

[41] Anupam K. Chakravarty and Daniel F. Jarosz. More than Just a Phase: Prions at the Crossroads of Epigenetic Inheritance and Evolutionary Change, nov 2018.

[42] John R. Glover, Anthony S. Kowal, Eric C. Schirmer, Maria M. Patino, Jia Jia Liu, and Susan Lindquist. Self-seeded fibers formed by Sup35, the protein determinant of [PSI+], a heritable prion-like factor of S. cerevisiae. *Cell*, 89(5):811–819, may 1997. doi: 10.1016/S0092-8674(00)80264-0.

[43] Yury O. Chernoff, Susan L. Lindquist, Bun Ichiro Ono, Sergei G. Inge-Vechtomov, and Susan W. Liebman. Role of the chaperone protein Hsp104 in propagation of the yeast prion-like factor [psi+]. *Science (80-.).*, 268(5212):880–884, may 1995. doi: 10.1126/science.7754373.

[44] James Shorter and Susan Lindquist. Prions as adaptive conduits of memory and inheritance, jun 2005.

[45] Ricardo Marchante, David M. Beal, Nadejda Koloteva-Levine, Tracey J. Purton, Mick F. Tuite, and Wei Feng Xue. The physical dimensions of amyloid aggregates control their infective potential as prion particles. *Elife*, 6, sep 2017. doi: 10.7554/ELIFE.27109.

[46] Claudia Scheckel and Adriano Aguzzi. Prions, prionoids and protein misfolding disorders. *Nat. Rev. Genet. 2018 197*, 19(7):405–418, apr 2018. doi: 10.1038/s41576-018-0011-4.

[47] S. V. Paushkin, V. V. Kushnirov, V. N. Smirnov, and M. D. Ter-Avanesyan. Propagation of the yeast prion-like [psi+] determinant is mediated by oligomerization of the SUP35-encoded polypeptide chain release factor. *EMBO J.*, 15(12):3127–3134, jun 1996. doi: 10.1002/J.1460-2075.1996.TB00675.X.

[48] Vitaly V Kushnirov and Michael D Ter-Avanesyan. Structure and Replication of Yeast Prions. *Cell*, 94(1):13–16, jul 1998. doi: 10.1016/S0092-8674(00)81216-7.

[49] Renee D. Wegrzyn, Kavita Bapat, Gary P. Newnam, Amy D. Zink, and Yury O. Chernoff. Mechanism of Prion Loss after Hsp104 Inactivation in Yeast. *Mol. Cell. Biol.*, 21(14):4656–4669, jul 2020. doi: 10.1128/MCB.21.14.4656-4669.2001.

[50] Heather L. True and Susan L. Lindquist. A yeast prion provides a mechanism for genetic variation and phenotypic diversity. *Nature*, 407(6803):477–483, sep 2000. doi: 10.1038/35035005.

[51] Andy H. Yuan and Ann Hochschild. A bacterial global regulator forms a prion. *Science (80-.).*, 355(6321), jan 2017. doi: 10.1126/science.aai7776.

[52] Tomasz Zajkowski, Michael D Lee, Shamba S Mondal, Amanda Carbajal, Robert Dec, Patrick D Brennock, Radoslaw W Piast, Jessica E Snyder, Nicholas B Bense, Wojciech Dzwolak, Daniel F Jarosz, and Lynn J Rothschild. The Hunt for Ancient Prions: Archaeal Prion-Like Domains Form Amyloid-Based Epigenetic Elements. *Mol. Biol. Evol.*, 38(5):2088–2103, may 2021. doi: 10.1093/molbev/msab010.

[53] Heather L. True, Ilana Bedin, and Susan L. Lindquist. Epigenetic regulation of translation reveals hidden genetic variation to produce complex traits. *Nature*, 431 (7005):184–187, sep 2004. doi: 10.1038/nature02885.

[54] Olivier Namy, Aurélie Galopier, Cyrielle Martini, Senya Matsufuji, Céline Fabret, and Jean Pierre Rousset. Epigenetic control of polyamines by the prion [PSI+]. *Nat. Cell Biol.*, 10(9):1069–1075, 2008. doi: 10.1038/ncb1766.

[55] Tatyana Rogoza, Alexander Goginashvili, Sofia Rodionova, Maxim Ivanov, Olga Viktorovskaya, Alexander Rubel, Kirill Volkov, and Ludmila Mironova. Non-Mendelian determinant [ISP+] in yeast is a nuclear-residing prion form of the global transcriptional regulator Sfp1. *Proc. Natl. Acad. Sci. U. S. A.*, 107(23):10573–10577, jun 2010. doi: 10.1073/pnas.1005949107.

[56] Alex K. Lancaster, J. Patrick Bardill, Heather L. True, and Joanna Masel. The spontaneous appearance rate of the yeast prion [PSI+] and its implications for the evolution of the evolvability properties of the [PSI+] system. *Genetics*, 184(2):393–400, feb 2010. doi: 10.1534/genetics.109.110213.

[57] Jens Tyedmers, Maria Lucia Madariaga, and Susan Lindquist. Prion switching in response to environmental stress. *PLoS Biol.*, 6(11):2605–2613, nov 2008. doi: 10.1371/journal.pbio.0060294.

[58] Genjiro Suzuki, Naoyuki Shimazu, and Motomasa Tanaka. A yeast prion, Mod5, promotes acquired drug resistance and cell survival under environmental stress. *Science*, 336(6079):355–359, apr 2012. doi: 10.1126/SCIENCE.1219491.

[59] Susan W. Liebman and Yury O. Chernoff. Prions in yeast, aug 2012.

[60] Christopher M. Jakobson and Daniel F. Jarosz. Organizing biochemistry in space and time using prion-like self-assembly. *Curr. Opin. Syst. Biol.*, 8:16, apr 2018. doi: 10.1016/J.COISB.2017.11.012.

[61] Mick F. Tuite and Tricia R. Serio. The prion hypothesis: from biological anomaly to basic regulatory mechanism. *Nat. Rev. Mol. Cell Biol.*, 11(12):823, dec 2010. doi: 10.1038/NRM3007.

[62] Shon A. Levkovich, Sigal Rencus-Lazar, Ehud Gazit, and Dana Laor Bar-Yosef. Microbial Prions: Dawn of a New Era. *Trends Biochem. Sci.*, 46(5):391–405, may 2021. doi: 10.1016/J.TIBS.2020.12.006.

[63] Motomasa Tanaka, Peter Chien, Nariman Naber, Roger Cooke, and Jonathan S. Weissman. Conformational variations in an infectious protein determine prion strain differences. *Nat. 2004 4286980*, 428(6980):323–328, mar 2004. doi: 10.1038/nature02392.

[64] Marie Lise Maddelein, Suzana Dos Reis, Stéphane Duvezin-Caubet, Bénédicte Coulary-Salin, and Sven J. Saupe. Amyloid aggregates of the HET-s prion protein are infectious. *Proc. Natl. Acad. Sci.*, 99(11):7402–7407, may 2002. doi: 10.1073/PNAS.072199199.

[65] Eleanor Fleming, Andy H. Yuan, Danielle M. Heller, and Ann Hochschild. A bacteria-based genetic assay detects prion formation. *Proc. Natl. Acad. Sci. U. S. A.*, 116(10):4605–4610, mar 2019. doi: 10.1073/pnas.1817711116.

[66] Alan K. Itakura, Anupam K. Chakravarty, Christopher M. Jakobson, and Daniel F. Jarosz. Widespread Prion-Based Control of Growth and Differentiation Strategies in Saccharomyces cerevisiae. *Mol. Cell*, 77(2):266–278.e6, jan 2020. doi: 10.1016/J.MOLCEL.2019.10.027.

[67] Luana Fioriti, Cory Myers, Yan You Huang, Xiang Li, Joseph S. Stephan, Pierre Trifilieff, Luca Colnaghi, Stylianos Kosmidis, Bettina Drisaldi, Elias Pavlopoulos, and Eric R. Kandel. The Persistence of Hippocampal-Based Memory Requires Protein

Synthesis Mediated by the Prion-like Protein CPEB3. *Neuron*, 86(6):1433–1448, jun 2015. doi: 10.1016/j.neuron.2015.05.021.

[68] Sohini Chakrabortee, Can Kayatekin, Greg A. Newby, Marc L. Mendillo, Alex Lancaster, and Susan Lindquist. Luminidependens (LD) is an Arabidopsis protein with prion behavior. *Proc. Natl. Acad. Sci. U. S. A.*, 113(21):6065, may 2016. doi: 10.1073/PNAS.1604478113.

[69] Shaun H. Speldewinde and Chris M. Grant. The frequency of yeast [PSI+] prion formation is increased during chronological ageing. *Microb. Cell*, 4(4):127, apr 2017. doi: 10.15698/MIC2017.04.568.

[70] Irina L. Derkatch, Michael E. Bradley, Ping Zhou, Yury O. Chernoff, and Susan W. Liebman. Genetic and Environmental Factors Affecting the de novo Appearance of the [PSI +] Prion in Saccharomyces cerevisiae. *Genetics*, 147(2), 1997.

[71] Wickner RB. [URE3] as an altered URE2 protein: evidence for a prion analog in Saccharomyces cerevisiae. *Science*, 264(5158):566–569, 1994. doi: 10.1126/SCIENCE.7909170.

[72] Irina L. Derkatch, Michael E. Bradley, Sherie V.L. Masse, Sergei P. Zadorsky, Gennady V. Polozkov, Sergei G. Inge-Vechtomov, and Susan W. Liebman. Dependence and independence of [PSI+] and [PIN+]: a two-prion system in yeast? *EMBO J.*, 19 (9):1942–1952, may 2000. doi: 10.1093/EMBOJ/19.9.1942.

[73] Irina L. Derkatch, Michael E. Bradley, Joo Y. Hong, and Susan W. Liebman. Prions Affect the Appearance of Other Prions: The Story of [PIN+]. *Cell*, 106(2):171–182, jul 2001. doi: 10.1016/S0092-8674(01)00427-5.

[74] Lev Z Osherovich and Jonathan S Weissman. Multiple Gln/Asn-Rich Prion Domains Confer Susceptibility to Induction of the Yeast [PSI+] Prion. *Cell*, 106(2):183–194, jul 2001. doi: 10.1016/S0092-8674(01)00440-8.

[75] Sean J. Garrity, Viknesh Sivanathan, Jijun Dong, Susan Lindquist, and Ann Hochschild. Conversion of a yeast prion protein to an infectious form in bacteria. *Proc. Natl. Acad. Sci.*, 107(23):10596–10601, jun 2010. doi: 10.1073/PNAS.0913280107.

[76] Andy H. Yuan, Sean J. Garrity, Entela Nako, and Ann Hochschild. Prion propagation can occur in a prokaryote and requires the ClpB chaperone. *Elife*, 3(August2014):1–19, aug 2014. doi: 10.7554/eLife.02949.

[77] AK Lancaster, A Nutter-Upham, S Lindquist, and OD King. PLAAC: a web and command-line application to identify proteins with prion-like amino acid composition. *Bioinformatics*, 30(17):2501–2502, sep 2014. doi: 10.1093/BIOINFORMATICS/BTU310.

[78] Jerome P. Horwitz, Jonathan Chua, Ronald J. Curby, Arthur J. Tomson, Margaret A. Da Rooge, Benjamin E. Fisher, Jose Mauricio, and Irwin Klundt. Substrates for Cytochemical Demonstration of Enzyme Activity. I. Some Substituted 3-Indolyl-β-D-glycopyranosides1a. *J. Med. Chem.*, 7(4):574–575, jul 1964. doi: 10.1021/JM00334A044.

[79] Jeffrey H. Miller. Genetic studies of the lac repressor: XI. On aspects of lac repressor structure suggested by genetic experiments. *J. Mol. Biol.*, 131(2):249–258, jun 1979. doi: 10.1016/0022-2836(79)90075-5.

[80] Julian Davies and François Jacob. Genetic mapping of the regulator and operator genes of the lac operon. *J. Mol. Biol.*, 36(3):413–417, sep 1968. doi: 10.1016/0022-2836(68)90165-4.

[81] Douglas H Juers, Brian W Matthews, and Reuben E Huber. LacZ β-galactosidase: Structure and function of an enzyme of historical and molecular biological importance. *Protein Sci.*, 21(12):1792, dec 2012. doi: 10.1002/PRO.2165.

[82] Kryndushkin DS, Alexandrov IM, Ter-Avanesyan MD, and Kushnirov VV. Yeast [PSI+] prion aggregates are formed by small Sup35 polymers fragmented by Hsp104. *J. Biol. Chem.*, 278(49):49636–49643, 2003. doi: 10.1074/JBC.M307996200.

[83] Sviatoslav N. Bagriantsev, Vitaly V. Kushnirov, and Susan W. Liebman. Analysis of Amyloid Aggregates Using Agarose Gel Electrophoresis. *Methods Enzymol.*, 412:33–48, jan 2006. doi: 10.1016/S0076-6879(06)12003-0.

[84] John Collinge and Anthony R. Clarke. A General Model of Prion Strains and Their Pathogenicity. *Science (80-.).*, 318(5852):930–936, nov 2007. doi: 10.1126/SCIENCE.1138718.

[85] Lois E. Greene, Farrin Saba, Rebecca E. Silberman, and Xiaohong Zhao. Mechanisms for Curing Yeast Prions. *Int. J. Mol. Sci. 2020, Vol. 21, Page 6536*, 21(18):6536, sep 2020. doi: 10.3390/IJMS21186536.

[86] Dorweiler JE, Obaoye JO, Oddo MJ, Shilati FM, Scheidemantle GM, Coleman TJ, Reilly JA, Smith GR, and Manogaran AL. DMSO-mediated curing of several yeast prion variants involves Hsp104 expression and protein solubilization, and is decreased in several autophagy related gene (atg) mutants. *PLoS One*, 15(3), 2020. doi: 10.1371/JOURNAL.PONE.0229796.

[87] Courtney L. Klaips, Megan L. Hochstrasser, Christine R. Langlois, and Tricia R. Serio. Spatial quality control bypasses cell-based limitations on proteostasis to promote prion curing. *Elife*, 3, 2014. doi: 10.7554/ELIFE.04288.

[88] Guo Chiuan Hung and Daniel C. Masison. N-Terminal Domain of Yeast Hsp104 Chaperone Is Dispensable for Thermotolerance and Prion Propagation but Necessary for Curing Prions by Hsp104 Overexpression. *Genetics*, 173(2):611, 2006. doi: 10.1534/GENETICS.106.056820.

[89] Behrooz Moosavi, Jintana Wongwigkarn, and Mick F. Tuite. Hsp70/Hsp90 co-chaperones are required for efficient Hsp104-mediated elimination of the yeast [PSI(+)] prion but not for prion propagation. *Yeast*, 27(3):167–179, mar 2010. doi: 10.1002/YEA.1742.

[90] Michael Reidy and Daniel C. Masison. Sti1 Regulation of Hsp70 and Hsp90 Is Critical for Curing of Saccharomyces cerevisiae [PSI+] Prions by Hsp104. *Mol. Cell. Biol.*, 30 (14):3542, jul 2010. doi: 10.1128/MCB.01292-09.

[91] Gary P. Newnam, Jennifer L. Birchmore, and Yury O. Chernoff. Destabilization and Recovery of a Yeast Prion after Mild Heat Shock. *J. Mol. Biol.*, 408(3):432–448, may 2011. doi: 10.1016/J.JMB.2011.02.034.

[92] Michael B. Elowitz, Arnold J. Levine, Eric D. Siggia, and Peter S. Swain. Stochastic gene expression in a single cell. *Science (80-.).*, 297(5584):1183–1186, aug 2002. doi: 10.1126/science.1070919.

[93] Stephan Uphoff, Nathan D. Lord, Burak Okumus, Laurent Potvin-Trottier, David J. Sherratt, and Johan Paulsson. Stochastic activation of a DNA damage response causes cell-to-cell mutation rate variation. *Science (80-.).*, 351(6277):1094–1097, mar 2016. doi: 10.1126/science.aac9786.

[94] Arjun Raj and Alexander van Oudenaarden. Nature, Nurture, or Chance: Stochastic Gene Expression and Its Consequences, oct 2008.

[95] Johan Paulsson. Models of stochastic gene expression, jun 2005.

[96] James C.W. Locke and Michael B. Elowitz. Using movies to analyse gene circuit dynamics in single cells, 2009.

[97] Jeffrey R. Moffitt, Jeffrey B. Lee, and Philippe Cluzel. The single-cell chemostat: An agarose-based, microfluidic device for high-throughput, single-cell studies of bacteria and bacterial communities. *Lab Chip*, 12(8):1487–1494, apr 2012. doi: 10.1039/c2lc00009a.

[98] Da Yang, Anna D. Jennings, Evalynn Borrego, Scott T. Retterer, and Jaan Männik. Analysis of factors limiting bacterial growth in PDMS mother machine devices. *Front. Microbiol.*, 9(MAY):871, may 2018. doi: 10.3389/fmicb.2018.00871.

[99] Laurent Potvin-Trottier, Scott Luro, and Johan Paulsson. Microfluidics and single-cell microscopy to study stochastic processes in bacteria, jun 2018.

[100] Ping Wang, Lydia Robert, James Pelletier, Wei Lien Dang, Francois Taddei, Andrew Wright, and Suckjoon Jun. Robust growth of escherichia coli. *Curr. Biol.*, 20(12): 1099–1103, jun 2010. doi: 10.1016/j.cub.2010.04.045.

[101] Dong Qin, Younan Xia, John A. Rogers, Rebecca J. Jackman, Xiao-Mei Zhao, and George M. Whitesides. Microfabrication, Microstructures and Microsystems. pages 1–20. 1998. doi: 10.1007/3-540-69544-3_1.

[102] Henrik Bruus. Theoretical microfluidics. *Choice Rev. Online*, 45(10):45–5602–45–5602, 2008. doi: 10.5860/choice.45-5602.

[103] Brian J Kirby. *Micro- and Nanoscale Fluid Mechanics: Transport in Microfluidic Devices*. 2010. doi: 10.1007/s13398-014-0173-7.2.

[104] Sattar Taheri-Araghi, Steven D. Brown, John T. Sauls, Dustin B. McIntosh, and Suckjoon Jun. Single-Cell Physiology. *Annu. Rev. Biophys.*, 44:123–142, jun 2015. doi: 10.1146/annurev-biophys-060414-034236.

[105] Manuel Campos, Ivan V. Surovtsev, Setsu Kato, Ahmad Paintdakhi, Bruno Beltran, Sarah E. Ebmeier, and Christine Jacobs-Wagner. A constant size extension drives bacterial cell size homeostasis. *Cell*, 159(6):1433–1446, dec 2014. doi: 10.1016/j.cell.2014.11.022.

[106] Frederick K. Balagaddé, Lingchong You, Carl L. Hansen, Frances H. Arnold, and Stephen R. Quake. Microbiology: Long-term monitoring of bacteria undergoing programmed population control in a microchemostat. *Science (80-.).*, 309(5731): 137–140, jul 2005. doi: 10.1126/science.1109173.

[107] Diane Longo and Jeff Hasty. Dynamics of single-cell gene expression, may 2006.

[108] Yuichi Taniguchi, Paul J. Choi, Gene Wei Li, Huiyi Chen, Mohan Babu, Jeremy Hearn, Andrew Emili, and X. Sunney Xie. Quantifying E. coli proteome and transcriptome with single-molecule sensitivity in single cells. *Science (80-.).*, 329(5991):533–538, jul 2010. doi: 10.1126/science.1188308.

[109] Mats Wallden and Johan Elf. Studying transcriptional interactions in single cells at sufficient resolution, feb 2011.

[110] Jeongyun Kim, Manjunath Hegde, and Arul Jayaraman. Co-culture of epithelial cells and bacteria for investigating host-pathogen interactions. *Lab Chip*, 10(1):43–50, jan 2010. doi: 10.1039/b911367c.

[111] Nathalie Q. Balaban, Jack Merrin, Remy Chait, Lukasz Kowalik, and Stanislas Leibler. Bacterial persistence as a phenotypic switch. *Science (80-.).*, 305(5690):1622–1625, sep 2004. doi: 10.1126/science.1099390.

[112] Heon Ho Jeong, Si Hyung Jin, Byung Jin Lee, Taesung Kim, and Chang Soo Lee. Microfluidic static droplet array for analyzing microbial communication on a population gradient. *Lab Chip*, 15(3):889–899, feb 2015. doi: 10.1039/c4lc01097c.

[113] Aimee K. Wessel, Laura Hmelo, Matthew R. Parsek, and Marvin Whiteley. Going local: Technologies for exploring bacterial microenvironments, may 2013.

[114] M.S. Ferry, I.A. Razinkov, and J. Hasty. Microfluidics for Synthetic Biology. volume 497, pages 295–372. Academic Press, jan 2011. doi: 10.1016/b978-0-12-385075-1.00014-7.

[115] Yujun Song, Daojian Cheng, Liang Zhao, Yujun Song, Xiaoxiong Zhao, Qingkun Tian, and Hongxia Liang. Fundamental Concepts and Physics in Microfluidics. In *Microfluid. Fundam. Devices Appl.*, pages 19–111. Wiley-VCH Verlag GmbH & Co. KGaA, Weinheim, Germany, jan 2018. doi: 10.1002/9783527800643.ch2.

[116] Osborne Reynolds. XXIX. An experimental investigation of the circumstances which determine whether the motion of water shall be direct or sinuous, and of the law of

resistance in parallel channels. *Philos. Trans. R. Soc. London*, 174:935–982, dec 1883. doi: 10.1098/rstl.1883.0029.

[117] N Rott. NOTE ON THE HISTORY OF THE REYNOLDS NUMBER. Technical report, 1990.

[118] Neil Convery and Nikolaj Gadegaard. 30 years of microfluidics, mar 2019.

[119] Fallahi H, Zhang J, Phan HP, and Nguyen NT. Flexible Microfluidics: Fundamentals, Recent Developments, and Applications. *Micromachines*, 10(12), dec 2019. doi: 10.3390/MI10120830.

[120] Samuel K. Sia and George M. Whitesides. Microfluidic devices fabricated in poly(dimethylsiloxane) for biological studies, nov 2003.

[121] Yung Kuang Yang and Tsun Ching Chang. Experimental analysis and optimization of a photo resist coating process for photolithography in wafer fabrication. *Microelectronics J.*, 37(8):746–751, aug 2006. doi: 10.1016/j.mejo.2005.10.006.

[122] Jay W. Lathrop. The diamond ordnance fuze laboratory's photolithographic approach to microcircuits. *IEEE Ann. Hist. Comput.*, 35(1):48–55, 2013. doi: 10.1109/MAHC.2011.83.

[123] Microchem. SU-8 2000 Permanent Epoxy Negative Photoresist. Technical report.

[124] H. Fraser and A. G. Dickinson. Scrapie in mice: Agent-strain differences in the distribution and intensity of grey matter vacuolation. *J. Comp. Pathol.*, 83(1):29–40, jan 1973. doi: 10.1016/0021-9975(73)90024-8.

[125] Timothy S. Vaughan. In search of the memoryless property. *Proc. - Winter Simul. Conf.*, pages 2572–2576, 2008. doi: 10.1109/WSC.2008.4736369.

[126] Dirk Landgraf, Burak Okumus, Peter Chien, Tania A. Baker, and Johan Paulsson. Segregation of molecules at cell division reveals native protein localization. *Nat. Methods*, 9(5):480–482, may 2012. doi: 10.1038/NMETH.1955.

[127] Dann Huh and Johan Paulsson. Non-genetic heterogeneity from stochastic partitioning at cell division. *Nat. Genet. 2010 432*, 43(2):95–100, dec 2010. doi: 10.1038/ng.729.

[128] Stanley B. Prusiner. Molecular biology of prion diseases. *Science*, 252(5012):1515–1522, 1991. doi: 10.1126/SCIENCE.1675487.

[129] Sander K. Govers, Julien Mortier, Antoine Adam, and Abram Aertsen. Protein aggregates encode epigenetic memory of stressful encounters in individual Escherichia coli cells. *PLOS Biol.*, 16(8):e2003853, aug 2018. doi: 10.1371/JOURNAL.PBIO.2003853.

[130] Antoine G. Godin, Santiago Costantino, Louis Etienne Lorenzo, Jody L. Swift, Mikhail Sergeev, Alfredo Ribeiro-da Silva, Yves De Koninck, and Paul W. Wiseman. Revealing protein oligomerization and densities in situ using spatial intensity distribution analysis. *Proc. Natl. Acad. Sci. U. S. A.*, 108(17):7010–7015, apr 2011. doi: 10.1073/PNAS.1018658108/-/DCSUPPLEMENTAL.

[131] David A. Bateman and Reed B. Wickner. The [PSI+] Prion Exists as a Dynamic Cloud of Variants. *PLOS Genet.*, 9(1):e1003257, 2013. doi: 10.1371/JOURNAL.PGEN.1003257.

[132] Kahp Yang Suh, Sun Min Kim, Sung Hoon Lee, Min Cheol Park, Keon Woo Kwon, and Pilnam Kim. Soft lithography for microfluidics: a review. *BIOCHIP J.*, 2(1):1–11, 2008.

[133] Justin Wen. PDMS-Glass Bonding Protocol - Anatech. Technical report, 2015.

[134] Yusuke V. Morimoto, Shuichi Nakamura, Nobunori Kami-ike, Keiichi Namba, and Tohru Minamino. Charged residues in the cytoplasmic loop of MotA are required for stator assembly into the bacterial flagellar motor. *Mol. Microbiol.*, 78(5):1117–1129, dec 2010. doi: 10.1111/J.1365-2958.2010.07391.X.

[135] Thomas M. Norman, Nathan D. Lord, Johan Paulsson, and Richard Losick. Memory and modularity in cell-fate decision making. *Nat. 2013 5037477*, 503(7477):481–486, nov 2013. doi: 10.1038/nature12804.

[136] Markus Basan, Tomoya Honda, Dimitris Christodoulou, Manuel Hörl, Yu-Fang Chang, Emanuele Leoncini, Avik Mukherjee, Hiroyuki Okano, Brian R. Taylor, Josh M. Silverman, Carlos Sanchez, James R. Williamson, Johan Paulsson, Terence Hwa, and Uwe Sauer. A universal trade-off between growth and lag in fluctuating environments. *Nat. 2020 5847821*, 584(7821):470–474, jul 2020. doi: 10.1038/s41586-020-2505-4.

[137] Thomas Julou, Ludovit Zweifel, Diana Blank, Athos Fiori, and Erik van Nimwegen. Subpopulations of sensorless bacteria drive fitness in fluctuating environments. *PLOS Biol.*, 18(12):e3000952, dec 2020. doi: 10.1371/JOURNAL.PBIO.3000952.

[138] Guillaume Witz, Erik Van Nimwegen, and Thomas Julou. Initiation of chromosome replication controls both division and replication cycles in e. Coli though a double-adder mechanism. *Elife*, 8, nov 2019. doi: 10.7554/ELIFE.48063.

[139] Matthias Kaiser, Florian Jug, Thomas Julou, Siddharth Deshpande, Thomas Pfohl, Olin K. Silander, Gene Myers, and Erik van Nimwegen. Monitoring single-cell gene regulation under dynamically controllable conditions with integrated microfluidics and software. *Nat. Commun. 2018 91*, 9(1):1–16, jan 2018. doi: 10.1038/s41467-017-02505-0.

[140] Somenath Bakshi, Emanuele Leoncini, Charles Baker, Silvia J. Cañas-Duarte, Burak Okumus, and Johan Paulsson. Tracking bacterial lineages in complex and dynamic environments with applications for growth control and persistence. *Nat. Microbiol. 2021 66*, 6(6):783–791, may 2021. doi: 10.1038/s41564-021-00900-4.